Journal of Fluids and Structures 140 (2026) 104447

Contents lists available at ScienceDirect

Journal of Fluids and Structures

journal homepage: www.elsevier.com/locate/yjfls

Multiphysics analysis of a flexible oscillating water column wave energy converter with dielectric elastomer membrane

Yang Huang [a], Qing Xiao [a,*], Liu Yang [b], Saishuai Dai [a], Saeid Lotfian [a], Feargal Brennan [a]

[a] Department of Naval Architecture, Ocean & Marine Engineering, University of Strathclyde, Glasgow, UK
[b] Advanced Composite Group, Department of Mechanical and Aerospace Engineering, University of Strathclyde, Glasgow, UK

ARTICLE INFO

Keywords:
Flexible wave energy converter
Oscillating water column
Dielectric elastomer generator
Fluid-structure-electric interaction
Multiphysics simulation

ABSTRACT

Flexible wave energy converters (FlexWECs) have emerged as a promising solution to address the limitations of conventional rigid devices in harsh marine environments. Among them, oscillating water column (OWC) systems integrated with dielectric elastomer generators (DEGs) offer simplified architectures, enhanced adaptability, and direct wave-to-electric energy conversion. However, the complex multiphysics interactions between fluid, structure, and electric fields remain poorly understood, hindering design optimization and performance prediction. This study develops a high-fidelity computational framework to simulate the coupled fluid-structure-electric behaviour of a flexible OWC wave energy converter (WEC) with a DEG membrane. The framework is first validated against experimental data, demonstrating good agreement in capturing the deformation of the flexible membrane induced by the coupled electrostatic and hydrodynamic forces. Subsequently, the model is applied to investigate how electric field influences the WEC system behaviour under regular wave excitation. Results show that applying an electric field reduces the effective stiffness of the membrane, leading to increased deformation. Additionally, it does raise overall structural stress levels, especially near the membrane centre and edge regions, where the maximum stresses are observed. Notably, electric excitation induces a secondary deformation mode in the membrane during the near-flat phase. These effects become more pronounced with increasing initial voltage, which also leads to an approximately quadratic increase in output power. The insights gained from this study provide a deeper understanding of fluid-structure-electricity (FSE) interactions in flexible OWC WECs and offer design guidance for enhancing energy harvesting efficiency in next-generation WEC devices.

1. Introduction

As the global community accelerates its transition toward renewable energy, ocean wave energy is increasingly acknowledged as a promising and consistent energy resource with vast untapped potential (Hamedi et al., 2018; Aderinto and Li, 2018). Unlike solar and wind, wave energy offers high predictability and energy density. However, the practical deployment of conventional rigid wave energy converters (WECs) remains limited by persistent challenges in structural survivability, maintenance costs, and adaptability to dynamic and extreme sea states (Collins et al., 2021; Vertechy et al., 2014). To address these limitations, recent research has explored the use of

* Corresponding author.
E-mail address: qing.xiao@strath.ac.uk (Q. Xiao).

https://doi.org/10.1016/j.jfluidstructs.2025.104447
Received 30 July 2025; Received in revised form 20 October 2025; Accepted 28 October 2025

flexible and adaptive materials in WEC structures, aiming to enhance system resilience and efficiency by leveraging structural compliance (Kornbluh et al., 2012; Kaltseis et al., 2014).

Flexible wave energy converters (FlexWECs) represent an emerging class of devices designed to improve wave adaptability, structural integrity, and energy conversion efficiency (Collins et al., 2021). By integrating elastomeric components, particularly dielectric elastomer generators (DEGs), into the primary mover or power take-off (PTO) system, these devices simplify mechanical configurations and eliminate bulky transmission chains by direct electro-mechanical energy conversion. This direct-drive mechanism removes the need for conventional gearboxes and shafts, thereby reducing both system complexity and energy losses (Collins et al., 2021; Liu et al., 2020; Suo, 2010; Pelrine et al., 2001). Moreover, as fewer metallic components are exposed to seawater compared with traditional WECs, the DEG-based configuration exhibits improved corrosion resistance. DEGs enable direct electro-mechanical energy conversion, bypassing traditional rotary machinery and reducing both system complexity and energy losses (Suo, 2010; Pelrine et al., 2001). The inherent deformability of rubber-like materials also allows flexible structures to passively conform to wave-induced loads, offering potential advantages in adaptability, structural resilience, and long-term reliability under harsh marine conditions. Nevertheless, most FlexWEC concepts remain at the laboratory or prototype scale, and further validation under real-sea environments is required to substantiate these advantages.

Based on the architecture of energy harvesting, WEC systems can generally be divided into three subsystems (Collins et al., 2021): (a) the primary mover, which is responsible for extracting mechanical energy from wave motion, (b) the PTO, which converts mechanical motion into electrical energy, and (c) non-harvesting components such as structural supports and mooring lines. Each of these subsystems can potentially be replaced or enhanced by flexible structure designs. Over twenty FlexWEC concepts have been proposed, including devices like Sea-Clam (Peatfield et al., 1987), AWS-III (AWS, 2025), Bombora mWave (Orphin et al., 2017), and DrumWEC (Fontana et al., 2018) (using membranes as primary movers); PolyBuoy (Moretti et al., 2014) and PolySurge (Moretti et al., 2019; Moretti et al., 2020) (where DEGs serve as PTO units); and Qoceant or Symphony (AWS, 2025), which utilize membranes in auxiliary components.

Among the many WEC types, the oscillating water column (OWC) stands out for its mechanical simplicity and ease of maintenance (Vertechy et al., 2013; Rosati Papini et al., 2013; Falcão and Henriques, 2016). In a typical flexible OWC WEC, an enclosed air chamber interacts with incoming waves through a submerged opening at the base. A circular DEG diaphragm seals the top, undergoing cyclic upward and downward deformation driven by the internal air-water dynamics. The mechanical deformation of the DEG, in coordination with an external control circuit, generates electrical energy. This type of system, characterized by its compactness and adaptability, forms the foundation of our current research.

Several experimental and numerical efforts have been dedicated to validating and enhancing the performance of DEG-integrated OWC WECs. Theoretical models have been proposed to describe DEG behaviour under oscillatory loading, capturing key features such as hyperelasticity and viscoelasticity (Rosati Papini et al., 2013; Moretti et al., 2015). Reduced-order models have been used to simulate the dynamics of DEG-based PTOs and facilitate real-time control strategies (Vertechy et al., 2013; Moretti et al., 2018; Rosati Papini et al., 2018). Prototype-scale experiments, both in wave flumes and limited open-sea conditions, have confirmed the feasibility of DEG-based energy harvesting (Moretti et al., 2019; Moretti et al., 2020). Notably, the polymeric-OWC (Poly-OWC) and polymeric-axisymmetric OWC (Poly-A-OWC) configurations introduced modular architectures with DEG-based PTOs and demonstrated encouraging levels of power output and structural stability. Additionally, 1:20 scale experiments have explored how flexible materials influence dynamic response characteristics, highlighting the complex interplay between hydrodynamic loading and structural deformation (Abad et al., 2024).

Despite these advances, existing numerical studies largely rely on reduced-order models based on potential flow theory, which introduce significant simplifications (Rosati Papini et al., 2013; Moretti et al., 2015; Moretti et al., 2018; Rosati Papini et al., 2018; Schumacher et al., 2018). These models often assume spherical membrane deformation, uniform thickness distribution, and single-mode structural responses, making them inadequate for capturing localized flow features and high-order deformation behaviours. However, existing experimental and numerical studies suggest that flexible DEG membranes exhibit nonlinear and spatially non-uniform responses, with significant variations in local curvature, thickness, and stress concentrations across the surface (Wang et al., 2017; Huang et al., 2025). Furthermore, the surrounding flow field displays complex vortex structures and velocity gradients that cannot be resolved by simplified methods. Therefore, a high-fidelity multiphysics simulation framework is essential for accurately characterizing the coupled fluid-structure-electric interactions in such devices.

In our previous work, we developed a coupled computational fluid dynamics (CFD)-finite element analysis (FEA) solver to model the fluid-structure interaction of flexible OWC WECs under regular wave conditions (Huang et al., 2023). Building upon this, the present study extends the framework to incorporate electrical field modelling, enabling a comprehensive analysis of the fluid-structure-electric coupling behaviour of DEG-based FlexWECs. This extended multiphysics platform is used to investigate the influence of electricity field and initial voltage on the internal flow field, membrane deformation modes, stress distributions, and electrical output. The results provide critical insights into the design optimization and operational strategies for high-performance flexible OWC WECs.

This paper is organized as follows. Section 2 introduces the multiphysics computational framework for simulating fluid-structure-electric interactions. Section 3 presents the validation of the simulation tool. Section 4 describes the model setup, including the geometry, control circuitry, and wave conditions. Section 5 analyses the coupled dynamic responses of the WEC system under various wave frequencies and electrical inputs. Finally, Section 6 summarizes the main conclusions and outlines directions for future research.

2. Methodology

In our previous studies, we developed a coupled fluid-structure interaction (FSI) analysis framework that integrates CFD and FEA to simulate complex FSI problems (Huang et al., 2023). This framework has been successfully validated through several benchmark cases, including the interaction of a three-dimensional flexible plate in a uniform current and the deformation of a floating elastic disk subjected to regular waves, demonstrating its accuracy and robustness. It has also been applied to investigate the dynamic responses of flexible OWC WECs and flexible tube WECs (Huang et al., 2025; Huang et al., 2025).

In the present study, to investigate a novel concept of FlexWECs that integrates OWC technology with DEG membranes, the existing framework has been further extended by incorporating an electrostatic field solver. The resulting fluid-structure-electricity (FSE) framework enables comprehensive multiphysics analysis of the wave-induced dynamic behaviours of DEG-integrated FlexWECs. A brief description of this enhanced framework is provided in the following sub-section.

2.1. Fluid solver

Large-eddy simulation (LES) is employed to capture the transient viscous flow around the WEC. The flow field is governed by the three-dimensional incompressible Navier-Stokes equations, expressed as:

$$\frac{\partial \overline{u}_i}{\partial x_i} = 0, \tag{1}$$

$$\frac{\partial \rho \overline{u}_i}{\partial t} + \frac{\partial}{\partial x_j}\left[\rho \overline{u}_i\left(\overline{u}_j - \widehat{u}_j\right)\right] = -\frac{\partial \overline{p}_i}{\partial x_i} + \frac{\partial}{\partial x_j}\left[\mu_e\left(\frac{\partial \overline{u}_i}{\partial x_j} + \frac{\partial \overline{u}_j}{\partial x_i}\right)\right] - \frac{\partial \tau_{ij}}{\partial x_j} + \rho g_i + f_\sigma, \tag{2}$$

where x_i represents the Cartesian coordinates in the x, y, and z directions, $\overline{u}_i$ denotes the resolved filtered velocity component, ρ is the fluid density, $\overline{p}_i$ is the resolved filtered pressure, $\widehat{u}_j$ represents the mesh velocity. The effective dynamic viscosity is given by $\mu_e = \rho(\nu+\nu_t)$, where ν and ν_t are the kinematic and eddy viscosities, respectively. The terms g_i and f_σ represent the gravity acceleration and surface tension force, respectively.

The subgrid-scale (SGS) stress tensor $\tau_{ij} = \overline{u_i u_j} - \overline{u}_i \overline{u}_j$ is modelled using the standard Smagorinsky model (Smagorinsky, 1963), expressed as:

$$\tau_{ij} = -2\upsilon_S \overline{S}_{ij}, \tag{3}$$

$$\upsilon_S = (C_s\Delta)^2\left(2\overline{S}_{ij}\overline{S}_{ij}\right)^{1/2}, \overline{S}_{ij} = \frac{1}{2}\left(\frac{\partial \overline{u}_i}{\partial x_j} + \frac{\partial \overline{u}_j}{\partial x_i}\right) \tag{4}$$

where υ_S is the SGS eddy viscosity, and the spatial filter $\Delta = (\Delta x \Delta y \Delta z)^{1/3}$ is defined by the local grid resolution. The Smargorinsky coefficient C_s is set as 0.14, which lies within the typical range (0.1-0.18) reported in previous studies of free-surface and coastal flows (Deardorff, 1970; Christensen and Deigaard, 2001). This value provides a good balance between numerical stability and accurate representation of subgrid-scale dissipation for the present flow conditions.

Notably, both the air and water phases are treated as incompressible fluids in the present solver. This assumption is generally valid for low-Mach-number conditions where density variations are negligible, and has been adopted in previous numerical studies of FlexWECs (Huang et al., 2025; Huang et al., 2025). However, for certain configurations such as flexible OWC WECs, the air in the chamber may experience a degree of compressibility, which can lead to slight deviations between numerical predictions and physical behaviour. This aspect is further discussed in detail in Section 5.2.1.

The fluid domain is discretized using the finite volume method (FVM), and the volume of fluid (VOF) technique is adopted to capture the motion of the free surface. Pressure-velocity coupling is solved using the PIMPLE algorithm, which combines the PISO and SIMPLE schemes in OpenFOAM to ensure stable and efficient time integration of the coupled equations. For temporal discretization, a second-order Crank-Nicolson scheme is used to ensure accuracy in unsteady simulations. Convective terms are discretized using a second-order upwind scheme, while gradient terms are approximated with a second-order limited Gauss linear scheme to maintain both accuracy and numerical stability.

Regular incident waves are generated at the inlet boundary based on linear (first-order) Stokes wave theory. The free surface elevation η and velocity components u, v, w are defined as:

$$\eta = A_w \cos\left(k_x x + k_y y - \omega t + \psi\right), \tag{5}$$

$$\begin{cases} u = A_w \omega \dfrac{\cosh[k(h+z)]}{\sinh(kh)} \cos(\theta)\cos(\beta) \\ v = A_w \omega \dfrac{\cosh[k(h+z)]}{\sinh(kh)} \cos(\theta)\sin(\beta) \\ w = A_w \omega \dfrac{\sinh[k(h+z)]}{\sinh(kh)} \sin(\theta) \end{cases}, \tag{6}$$

where A_w is the wave amplitude, $\omega = 2\pi/T$ is the wave frequency, with T as the wave period. ψ is the initial wave phase, β is the incident wave angle, and k is the wave number with components $k_x = k\cos(\beta)$ and $k_y = k\sin(\beta)$. The variable h denotes the water depth, θ is the total phase angle, and x, y, z are spatial coordinates.

To minimize spurious wave reflections from the outlet boundary, an active wave absorption technique (Higuera et al., 2014; Higuera et al., 2014) is implemented. Unlike relaxation zone methods that require artificial extensions of the computational domain, this technique applies boundary-based correction, significantly reducing the computational cost. Its effectiveness has been demonstrated in our previous studies (Huang et al., 2025; Huang et al., 2025).

2.2. Structure solver

The motion of the DEG membrane is governed by the conservation of linear momentum, leading to the following partial differential equation derived from Newton's second law:

$$\rho_s \frac{\partial^2 \mathbf{U_s}}{\partial t^2} = \nabla \cdot \boldsymbol{\sigma} + \mathbf{f}, \tag{7}$$

where $\mathbf{U_s}$ denotes the displacement vector, ρ_s is the material density, $\boldsymbol{\sigma}$ is the Cauchy stress tensor, and $\mathbf{f}$ represents the body forces per unit volume.

To capture the nonlinear dynamic behaviour of the hyperelastic membrane, the governing equation is supplemented with a finite-strain kinematic relation and an appropriate constitutive model. In this work, the structure is treated as an incompressible hyperelastic material, and its mechanical response is described using the Mooney-Rivlin model (Mooney, 1940). The strain energy density function W is defined as:

$$W = C_1(\bar{I}_1 - 3) + C_2(\bar{I}_2 - 3), \tag{8}$$

where C_1 and C_2 are material constants, and $\bar{I}_1$ and $\bar{I}_2$ are the first and second invariants of the deviatoric right Cauchy-Green deformation tensor $\overline{\mathbf{C}}$. The Cauchy stress tensor is then derived from the strain energy function:

$$\boldsymbol{\sigma} = -p\mathbf{I} + 2\frac{\partial W}{\partial \overline{\mathbf{C}}}\mathbf{F}^{\mathrm{T}}\mathbf{F} \tag{9}$$

where $\mathbf{F}$ is the deformation gradient and p is a Lagrange multiplier that enforces the incompressibility condition, i.e., $\det(\mathbf{F}) = 1$.

The structural governing equations are discretized in space using a three-dimensional finite element method (FEM). Geometric nonlinearities are fully accounted for to ensure accurate modelling of large deformations, which are essential for simulating strong fluid-structure interactions. For time integration, the Newmark-β method (Newmark, 1959) is adopted. This implicit scheme is widely used for nonlinear dynamic analyses and provides unconditional stability in linear systems, making it well-suited for capturing the transient response of flexible structures under dynamic loading.

2.3. Electricity solver

In this study, a DEG membrane is employed as the PTO system. The DEG membrane is modelled as a compliant, deformable parallel-plate capacitor, in which the upper and lower surfaces of the elastomer membrane are coated with flexible electrodes. When an external voltage is applied, electrostatic forces are generated, inducing mechanical deformation of the membrane. In return, the resulting mechanical stretching modifies the electric field distribution, leading to a bidirectional electromechanical coupling.

The electrostatic force f_e acting on the membrane is derived from the Maxwell stress tensor under a quasi-static assumption. For a parallel-plate configuration, the electrostatic pressure applied normal to the membrane surface can be expressed as (Yan and Wong, 1993):

$$f_e = \frac{\varepsilon_0 \varepsilon_r V^2}{2{t_m}^2}, \tag{10}$$

where ε_0 is the vacuum permittivity, ε_r is the relative permittivity of the dielectric material, V is the applied voltage, and t_m is the instantaneous membrane thickness.

The voltage input $V(t)$ is defined according to a prescribed charge-discharge protocol, representing the operational control logic of the DEG circuit. A simple lumped-parameter electrical model is employed to simulate the PTO system. This model consists of a variable capacitor (associated with membrane deformation), a high-voltage power supply, a resistive load, and a set of switching elements. The timing and control of voltage application follow a typical energy harvesting cycle used in DEG-based systems (Falcão and Henriques, 2016). Further details are provided in Section 4.2.

2.4. Coupling strategy

The multiphysics coupling framework developed in this study integrates OpenFOAM (Jasak et al., 2007) for fluid dynamics,

CalculiX (Dhondt, 2017) for structural analysis, and the parallel-plate capacitor model (Yan and Wong, 1993) for calculating electrostatic forces. Data mapping and transfer among different physical domains are handled using the open-source coupling library preCICE (Degroote et al., 2009).

As illustrated in Fig. 1, a two-way coupling strategy is employed to model the interactions among the fluid, structural, and electrical fields. On one hand, the hydrodynamic and electrostatic forces are incorporated into the structural solver as external body forces acting normal to the membrane surface. On the other hand, the structural deformation influences both the flow field and the electric field: it modifies the boundary conditions in the fluid domain and alters the geometry of the membrane, thus affecting its capacitance and consequently the electrostatic force and energy output.

A partitioned coupling scheme is adopted to accommodate the use of different solvers and numerical methods for each physical domain. To enhance numerical stability and coupling accuracy, a strong coupling strategy is employed. An implicit time integration scheme is used to allow for relatively large time steps while maintaining stability and reducing computational cost. To further improve convergence efficiency, the IQN-ILS (Interface Quasi-Newton with Inverse Jacobian from a Least-Squares model) method (Degroote et al., 2009) is implemented to accelerate coupling iterations and damp oscillatory behaviour at the interface.

For inter-domain data transfer, radial basis function (RBF) interpolation is used to map nodal forces from the fluid and electrical domains to the structural mesh, while nodal displacements are transferred from the structural to the fluid and electrical domains (Lindner et al., 2017). The RBF method provides smooth, mesh-independent interpolation between non-conforming grids and offers high accuracy under large interface deformations, which makes it well suited for the present multiphysics coupling framework. Two mapping schemes are utilized within the RBF framework: a conservative scheme for force transfer, which ensures that the total transferred load is preserved across interfaces, and a consistent scheme for displacement transfer, which maintains pointwise geometric consistency by preserving the exact spatial correspondence of displacements between source and target nodes.

To evaluate convergence of the coupled system towards a monolithic solution, the discrete l_2-norm of the solution difference between consecutive iterations is computed. The simulation proceeds to the next time step once the convergence criterion is satisfied or when a predefined maximum number of iterations is reached.

3. Validation

3.1. Description of electrically activated membrane deformation

To validate the proposed FSE coupling framework, we simulate the deformation of a dielectric elastomer (DE) membrane under electrical activation and compare the results with experimental data reported by Fox and Goulbourne (Fox and Goulbourne, 2008). As illustrated in Fig. 2, a pre-stretched DE membrane is mounted onto a cylindrical chamber. The membrane's outer edge is clamped on the top of the chamber, and both sides are coated with compliant electrodes. A syringe connected to a linear stage is employed to inflate the membrane to a predetermined level, after which a sinusoidal voltage signal from a high-voltage power supply is applied. A pressure transducer and a laser vibrometer are used to monitor the internal chamber pressure and the membrane's central displacement, respectively. The main experimental parameters are summarized in Table 1, while additional details can be found in Fox and Goulbourne's study (Fox and Goulbourne, 2008).

In a typical test, the linear stage advances the syringe by a prescribed amount, inflating the membrane to a predefined volume (Fox and Goulbourne, 2008). Subsequently, a sinusoidal voltage signal $V(t)$ is applied to the DEG membrane as described below:

$$V(t) = V_0 \sin(2\pi f_v t) + V_0, \tag{11}$$

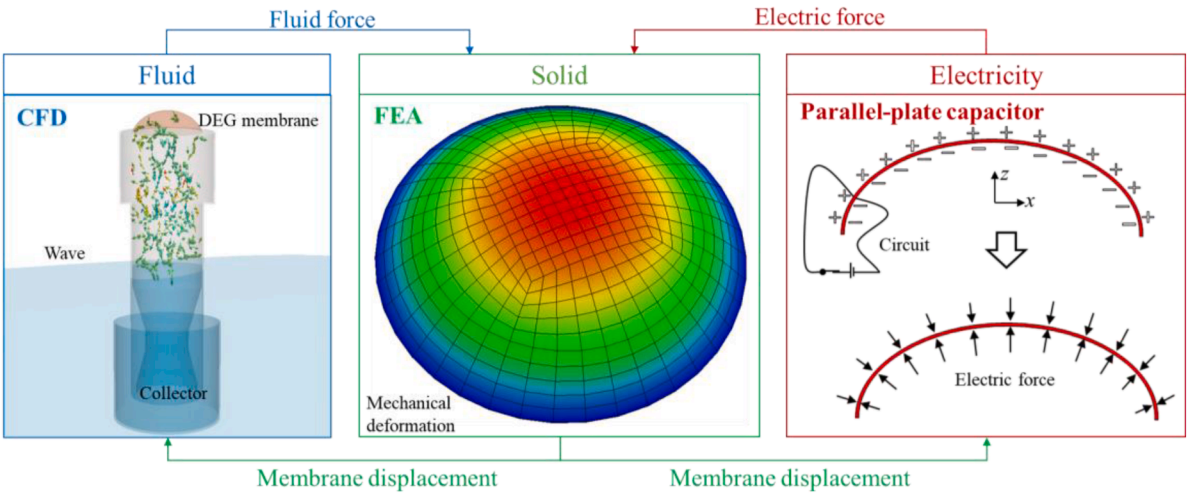

Fig. 1. Schematic diagram of two-way coupling for multiphysics simulations.

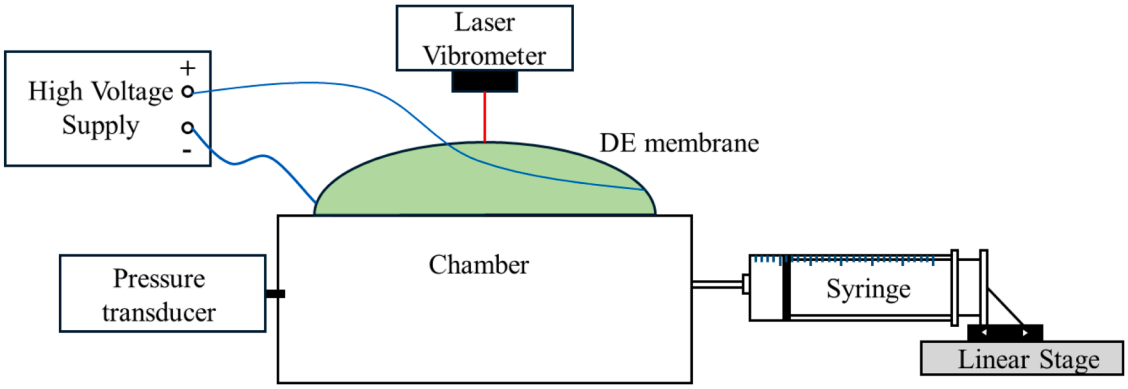

Fig. 2. Schematic of the experimental setup for the electrically activated membrane test.

Table 1
Key parameters for the electrically activated membrane experiment.

membrane material	Acrylic VHB 4905
Hyperelastic parameter	Mooney-Rivlin, $C_1 = 16$ kPa, $C_2 = 7.3$ kPa
Dielectric constant	$4.2 \times 8.85 \times 10^{-12}$ Fm^{-1}
Stretched membrane diameter	8.89 cm
Unstretched membrane thickness	0.5 mm
Pre-stretch	3
Chamber height	6.6 cm

where V_0 is half of the specified peak voltage, and f_v denotes the frequency of the applied signal.

For the present validation, two voltage conditions are considered: (a) $V_0 = 1$ kV, $f_v = 5$ Hz; (b) $V_0 = 2$ kV, $f_v = 100$ Hz. In both cases, the gas volume injected into the chamber via the syringe is fixed at 100 mL.

3.2. Comparison between numerical and experimental results

Figs. 3 and 4 present the time histories of membrane centre displacement and internal chamber pressure for the above two cases. As seen, both the membrane displacement and the chamber pressure exhibit periodic behaviours, with their variation periods matching that of the applied voltage signal. Comparison with experimental data shows good agreement, confirming that the proposed multi-physics analysis framework can accurately capture the dynamic behaviour of the DEG membrane under time-varying electrical excitation.

As mentioned earlier, the FSI module of the current framework has been validated and successfully applied to simulations of the same FlexWEC under regular wave conditions (Huang et al., 2023). Therefore, validation related to wave-induced responses is not repeated here. The newly developed integrated framework is subsequently employed to investigate the dynamic response of an OWC WEC incorporating a DEG membrane.

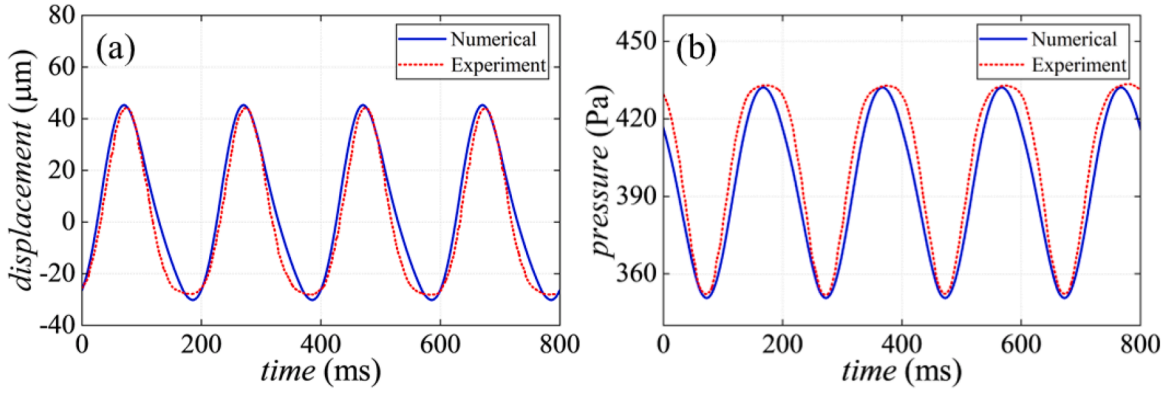

Fig. 3. Time histories of the DEG membrane response under harmonic voltage input with amplitude 1 kV and frequency 5 Hz: (a) Vertical displacement at the membrane centre; (b) Air-chamber pressure.

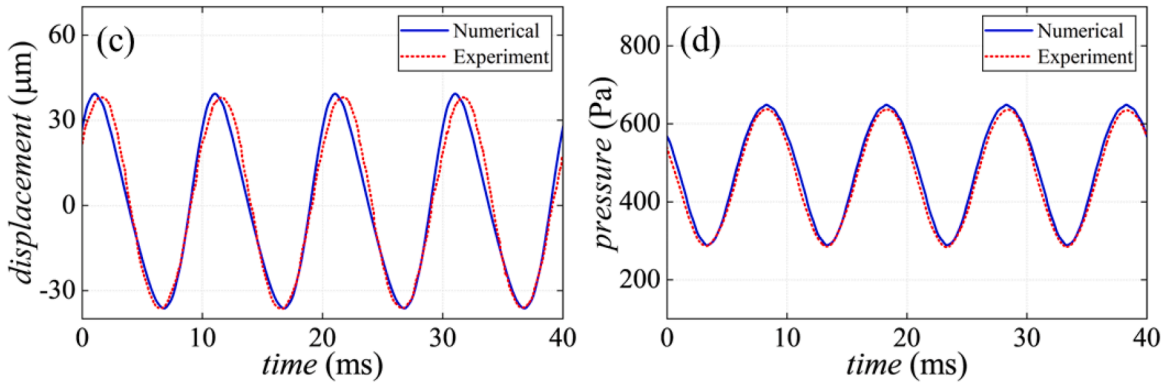

Fig. 4. Time histories of the DEG membrane response under harmonic voltage input with amplitude 2 kV and frequency 100 Hz: (a) Vertical displacement at the membrane centre; (b) Air-chamber pressure.

4. Numerical set up

4.1. Geometry model of OWC WEC

A representative FlexWEC, Poly-A-OWC integrated with a DEG membrane, originally proposed by Moretti et al. (Moretti et al., 2019), is selected for numerical analysis in this study. As illustrated in Fig. 5(a), the device primarily consists of a bottom U-shaped collector and a central cylindrical air chamber. The U-shaped collector design enables efficient wave capture and resonance tuning by extending the water column path, a concept originally introduced by Boccotti (Boccotti, 2003) and later implemented in practical devices such as the REWEC3 system (Liu et al., 2024). This configuration enhances the pneumatic pressure oscillations within the chamber, thereby improving the overall energy conversion efficiency. The top of the chamber is sealed with a circular diaphragm-type DEG membrane, consisting of two stacked layers of dielectric elastomer, with compliant electrodes coated on both external surfaces and at the interface between the two layers, resulting in three effective electrodes. Under periodic wave excitation, the membrane deforms up and down due to the differential pressure on the top and bottom surface of membrane. With the integration of a control circuit, the elastic potential energy stored in the membrane can be directly converted into electrical energy.

The key parameters of the DEG membrane are listed in Table 2. The longitudinal cross-section of the OWC model is shown in Fig. 5 (b), where the geometric dimensions are also indicated. Prior to installation at the chamber top, the DEG membrane is uniformly pre-stretched, as illustrated in Fig. 5(c). The pre-stretch ratio is defined as $\lambda_p = e_0/e$, where e_0 and e are the membrane radii before and after

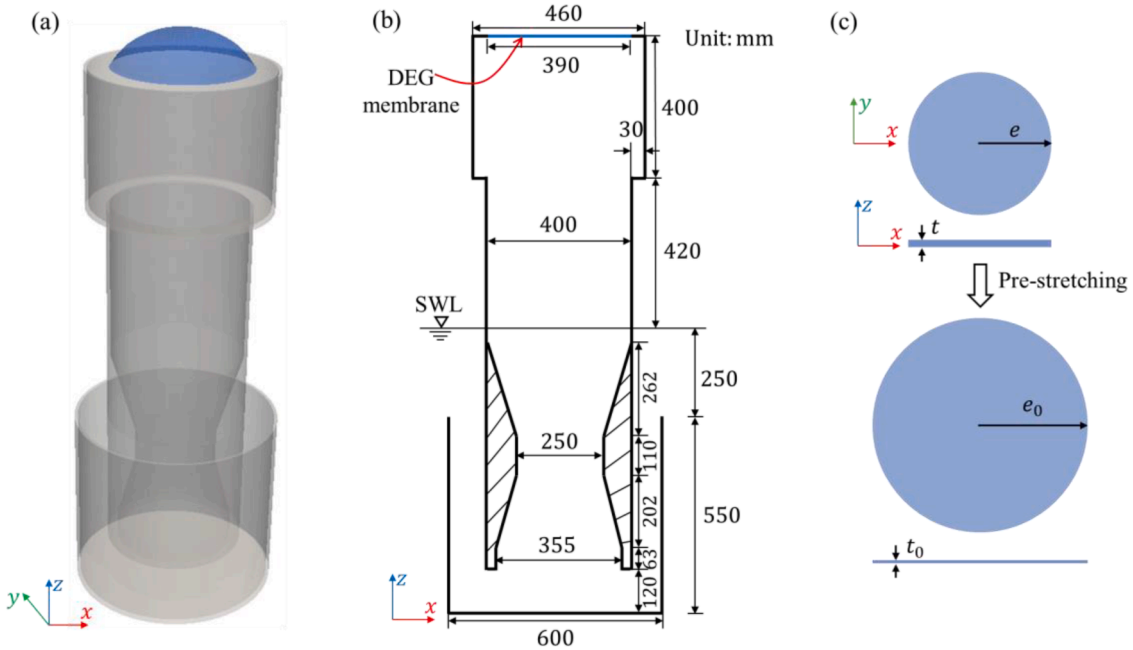

Fig. 5. (a) Schematic diagram of Poly-A-OWC model; (b) Longitudinal section of the model; (c) Pre-stretching of the DEG membrane.

Table 2
Main properties of DEG membrane in the flexible OWC WEC.

DEG membrane material	Acrylic VHB 4905
Hyperelastic parameter	Mooney-Rivlin, $C_1 = 5.5$ kPa, $C_2 = 0.57$ kPa
Dielectric constant	$4.2 \times 8.85 \times 10^{-12}$ Fm^{-1}
DEG membrane stretched diameter	0.39 m
DEG membrane unstretched thickness	2 mm
Pre-stretching	1.5

pre-stretching, respectively. Assuming the membrane is incompressible, the pre-stretched thickness can be determined from $t_0 = t/\lambda_p^2$, where t_0 and t denote the initial and pre-stretched membrane thicknesses, respectively.

Pre-stretching is commonly applied to dielectric elastomers to suppress wrinkling and pull-in instability, maintain a uniform tensile state, and enhance the effective electric field strength by reducing the membrane thickness. These effects collectively improve the electromechanical coupling efficiency and ensure stable deformation during cyclic loading. However, excessive pre-stretching may cause over-thinning and lead to numerical instability in the coupled fluid-structure-electric simulation (Jiang et al., 2016). a pre-stretching ratio of 1.5 is adopted in this study instead of the experimental value of 3.5 to maintain computational stability while adequately capturing the essential mechanical and dielectric responses of the membrane.

4.2. DEG and control circuit

To convert the elastic potential energy stored in the DEG membrane into electrical energy, an external control circuit and a dedicated control strategy are required. The circuit configuration adopted in the present study is adapted from the work of Moretti et al. (Moretti et al., 2019) and is illustrated in Fig. 6(a). In this setup, the DEG membrane is modelled as a variable capacitor C, which operates in parallel with a fixed capacitor $C_a = 394$ nF and is initially charged to a voltage of $V_0 = 4.5$ kV. The control circuit also includes three resistors (R_1, R_2, and R_3), three switches (S_1, S_2, and S_3), and a high-voltage (HV) power supply.

The energy harvesting process within each wave cycle is illustrated in Fig. 6(b), where the horizontal and vertical coordinates represent the charge (Q) and voltage (V) of the DEG membrane, respectively. The shaded area, denoted as W_e, corresponds to the electrical energy generated by the DEG membrane during a single conversion cycle. The complete power generation process consists of four phases, as described below:

(1) Expansion phase: At the onset of the cycle, as the DEG membrane undergoes deformation due to pressure variations, it is charged to the constant voltage V_0 via a high-voltage supply (S_1 closed; S_2, S_3 closed).
(2) Priming phase: Once the DEG membrane reaches its maximum capacitance C_A, S_1 is opened, and S_2 is closed, allowing the DEG and C_a to equilibrate their voltage V_A nearly instantaneously (S_1 open; S_2 closed; S_3 open).
(3) Harvesting phase: During membrane retraction, as its capacitance decreases, S_2 remains closed, and the DEG-C_a system is electrically isolated. In this stage, the total charge remains constant except for dielectric losses, allowing electrical energy to be extracted (S_1 open; S_2 closed; S_3 open).
(4) Discharging phase: When the membrane returns to its flat configuration, corresponding to the lowest capacitance C_B, S_2 is opened, and S_3 is closed, enabling the DEG to fully discharge through the resistive load R_3. The voltage on the DEG and C_a is V_B. The cycle then resets with the opening of S_3 (S_1, S_2 open; S_3 closed).

It is important to note that the DEG membrane contributes to energy generation only during the capacitance-decreasing phase. This is because only when the membrane contracts and its capacitance reduce does the system perform net positive electrical work. Consequently, the electric field exerts a force on the membrane solely during this contraction phase.

Based on the energy conversion process described above, the instantaneous power $p_e\ (t)$ generated by the DEG membrane can be

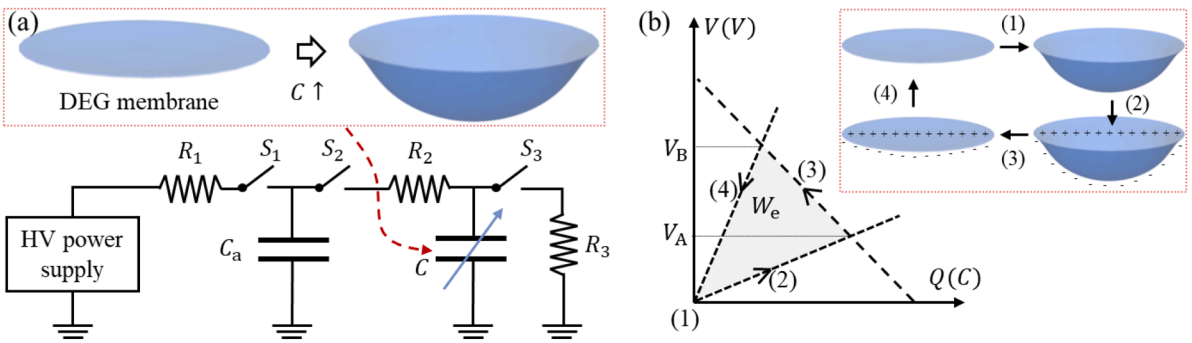

Fig. 6. (a) Control circuit for DEG PTO; (b) Schematic diagram of power generation in DEG membrane.

estimated as (Moretti et al., 2019):

$$p_e\ (t) = \frac{1}{2}C(t+\Delta t)V(t+\Delta t)^2 - \frac{1}{2}C(t)V(t)^2 + \frac{1}{2}C_a\left[V(t+\Delta t)^2 - V(t)^2\right] \tag{12}$$

where $C(t)$ and $V(t)$ denote the DEG membrane's capacitance and voltage at time t, respectively. The average electrical power $\overline{p}_e$ over one wave period T_w is given by:

$$\overline{p}_e = \frac{1}{T_w}\int_0^{T_w} p_e\ (t)\mathrm{d}t. \tag{13}$$

4.3. Computational domain and boundary conditions

A rectangular computational domain with dimensions of 4 m (length), 2 m (width), and 3.5 m (height) is established to simulate the flow field around the flexible OWC WEC, as illustrated in Fig. 7(a). The water depth is set to 2 m, and the height of the air phase is 1.5 m. The WEC is positioned at the centre of the domain, with a draft of 0.8 m. Although the distance between the model and the outlet boundary is relatively short (2 m), this setup is justified using an active wave absorption technique (Higuera et al., 2014; Higuera et al., 2014) at the outlet boundary, as discussed in Section 2.1. This approach effectively mitigates the influence of wave reflections,

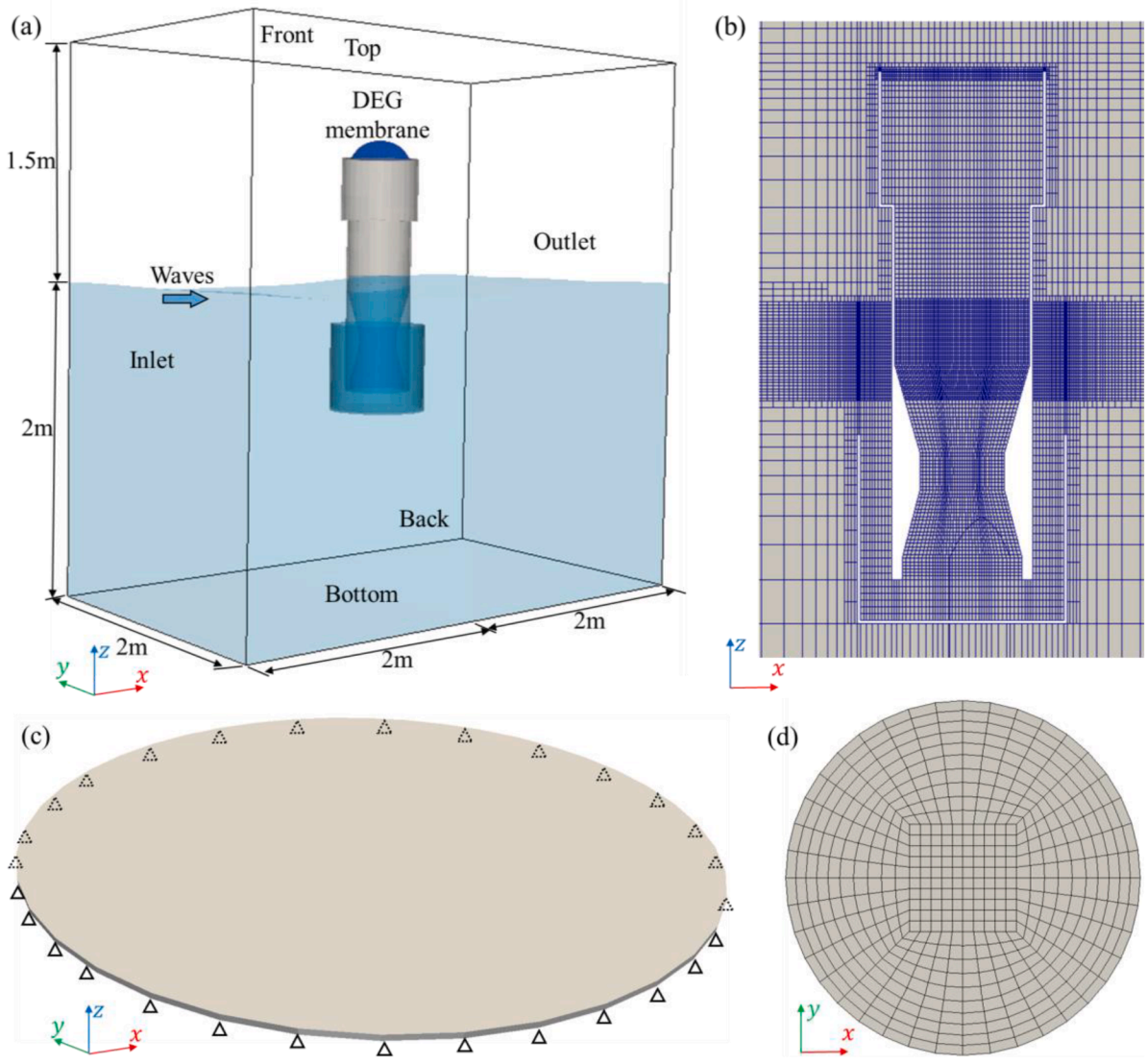

Fig. 7. (a) Computational domain for flow field; (b) Fluid mesh; (c) Computational model for flexible membrane; (d) Structure mesh.

therefore allowing a more compact computational domain without compromising simulation accuracy. This configuration has been validated in our previous study (Huang et al., 2025), where an identical setup successfully reproduced the target wave conditions with negligible reflection in the vicinity of the device.

Several monitoring points are deployed to record key physical quantities, including the incident wave amplitude, the free surface elevation at the OWC opening, the internal air pressure within the chamber, and the vertical displacement at the centre of the DEG membrane.

The mesh distribution around the WEC is shown in Fig. 7(b). To accurately capture the free surface and the membrane deformation, mesh refinement is applied in these regions. The minimum cell sizes are 2.0×10^{-3} m around the membrane and 5.0×10^{-3} m near the free surface. The total number of mesh elements in the computational domain is 1.81 million.

The boundary conditions applied are as follows: At the inlet, the velocity field is prescribed based on the incident wave parameters. A zero-gradient condition is imposed at the outlet, while the top boundary is treated as a pressure outlet. The bottom boundary is set as a no-slip wall, and symmetry boundary conditions are applied on the front and back faces of the domain.

For the structural simulation, only the flexible membrane is considered as the deformable component. As shown in Fig. 7(c), the membrane is clamped along its edge and undergoes periodic upward and downward deformations in response to fluid loading. The structural mesh consists of 1250 eight-node brick elements (C3D8) (Yan and Wong, 1993), as depicted in Fig. 7(d), and is used to resolve the membrane's deformation under coupled fluid-structure interaction.

To investigate the influence of regular waves, a range of wave frequencies is examined while maintaining a constant wave amplitude, with reference to the experimental study by Moretti et al. (Moretti et al., 2019). Three electric field scenarios are considered: (A) an FSI model without the electric field, serving as a baseline for comparison; (B) a fully coupled fluid-structure-electrical model with a constant applied voltage, used to evaluate the influence of the electric field on system responses; and (C) a parametric study involving varying voltage levels to assess their effect on resonance behaviour. A detailed summary of the simulation conditions is presented in Table 3.

5. Results and discussions

This section presents the coupled multiphysics responses of the OWC WEC equipped with a DEG membrane with various wave frequencies and applied voltages. Subsection 5.1 conducts mesh and time-step independence tests to determine the appropriate spatial and temporal resolutions for the simulations. Subsequently, Subsection 5.2 focuses on the system's response with resonant wave conditions, offering a detailed examination of the flow field, structural deformation, and electric field interactions. This provides an intuitive understanding of the coupled behaviour of the OWC WEC with a DEG membrane. The influence of wave frequency and applied voltage on the device's multiphysics responses are further explored in Subsections 5.3 and 5.4, respectively.

5.1. Mesh and time step sensitivity analysis

Three mesh resolutions were tested: coarse ($1.0 \times 10^{-2}D$), medium ($5.0 \times 10^{-3}D$), and fine grids ($2.5 \times 10^{-3}D$), where D denotes the membrane diameter. The corresponding total number of elements was approximately 1.27 million, 1.81 million, and 2.78 million, respectively. Additionally, a time-step sensitivity analysis was performed using $\Delta t = 2 \times 10^{-3}$ s, 1×10^{-3} s, and 5×10^{-4} s.

The tests were carried out under regular wave conditions with a period of 2.5 s and an amplitude of 0.05 m, along with an applied voltage of 4.5 kV. Fig. 8 show the temporal evolution of the normalized vertical displacement at the membrane centre d_z / A_w for different mesh sizes and time steps. Based on the results, the medium mesh provides a satisfactory balance between accuracy and computational cost, and a time step of 1×10^{-3} s was selected to ensure numerical stability in subsequent simulations.

5.2. Multiphysics responses of OWC WEC with DEG membrane

To better understand the coupled multiphysics behaviour of the OWC WEC integrated with a DEG membrane, a representative case is selected in which the membrane exhibits the maximum deformation under the resonant condition at $f_w = 0.4$ Hz. The interactions among fluid dynamics, structural responses, and electrical characteristics were examined to illustrate the coupled FSI-electric behaviour of the system.

5.2.1. Fluid dynamics

Wave interaction with the OWC WEC induces a free surface elevation difference between the external and internal flow fields, generating a pressure gradient. This pressure is transmitted through the air chamber to the membrane, causing its periodic defor-

Table 3
Summary of simulation conditions.

Lode case	Wave frequency f_w (Hz)	Wave amplitude A_w (m)	Electric field	Initial voltage V_0 (kV)
LC1	0.20~0.70	0.05	Off	0
LC2	0.20~0.70	0.05	On	4.5
LC3	0.40	0.05	On	1.5~4.5

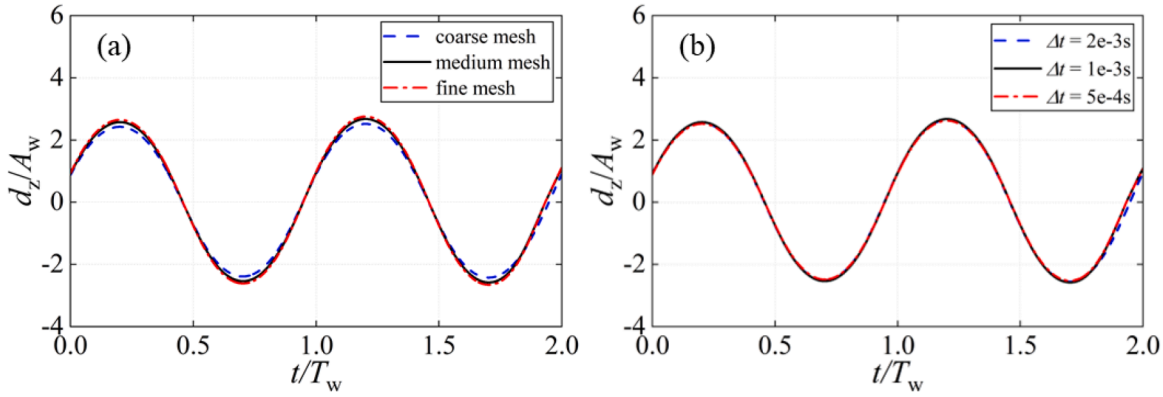

Fig. 8. Time histories of normalized vertical displacement at the membrane centre d_z/A_w: (a) Mesh convergence analysis; (b) Time-step sensitivity analysis.

mation. Fig. 9 illustrates the wave-structure interaction at resonance over one wave period (T_w). The free surface and air chamber are visualized in terms of wave elevation and dimensionless pressure $(p - p_a)/(\rho g A_w)$, with p_a denoting atmospheric pressure.

The membrane deforms periodically in response to wave loading. The pressure within the air chamber remains relatively uniform spatially. Notably, the pressure variation is not always in phase with membrane deformation. For instance, the pressure at $t = 0.625T_w$ is higher than at $t = 0.75T_w$, yet the deformation is smaller. This asynchronous behaviour will be discussed later.

To further explore the interaction between the DEG membrane and incident waves, time histories of key physical quantities are

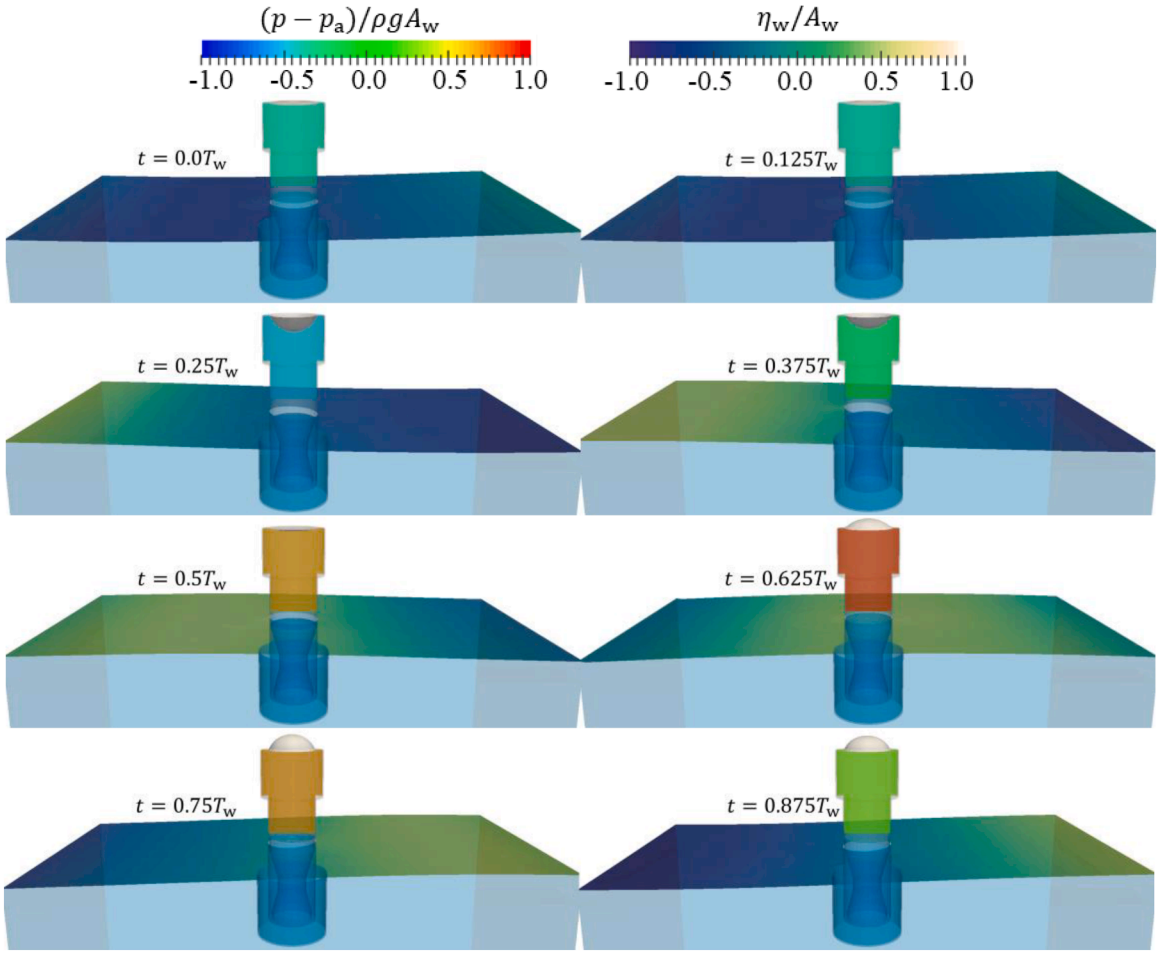

Fig. 9. FSI responses of the OWC WEC at selected time instants over one wave period in load case LC2 at resonant frequency $f_w = 0.4$ Hz.

plotted in Fig. 10. These include the wave elevation (η_w) measured 1 m in front of the OWC WEC, the water surface elevation (η_o) inside the collector, the air chamber pressure (p), the electric field-induced force on the membrane (f_e), and the vertical displacement at membrane centre (d_z). As seen, all quantities exhibit clear periodic behaviour. Notably, sudden jumps in air chamber pressure are observed at the moments when the electric field is switched on or off, as marked by red circles in Fig. 10(c), consistent with the experimental observations by Moretti et al. (Moretti et al., 2019). This phenomenon is attributed to a sudden reduction in membrane stiffness due to the applied voltage onto membrane.

It is worthy to note that the air compressibility is neglected in the present model, and thus air is treated as an incompressible fluid. This assumption is justified by the small pressure fluctuations observed in the OWC configuration. Based on the ideal gas law (Vertechy et al., 2014), the estimated volume change in the air chamber remains below 1% for all tested conditions and is therefore considered negligible.

It is observed that η_o and d_z are nearly in phase and both show a clear phase lag relative to the air chamber pressure (p), which is consistent with the observations in Fig. 9. To illustrate this phenomenon more clearly, the time histories of air chamber pressure and membrane displacement were fitted and compared in Fig. 11(a). The observed phase discrepancy arises from the dynamic coupling between the internal water column and the flexible membrane. Under the incompressible air assumption, the chamber pressure is not governed by volume changes but is instead determined by the requirement to satisfy the continuity of pressure and velocity at the air-water and air-membrane interfaces. As a result, the pressure response reflects the combined effects of fluid inertia and the membrane's elastic-inertial behaviour, leading to a noticeable phase lag relative to both the free surface and membrane motion.

When the air-water free surface drives the internal air motion, momentum is rapidly transferred to the membrane, triggering its deformation. Once the membrane has finite stiffness (e.g., due to pre-stretching), its response exhibits inertia and elastic restoring forces. The membrane not only passively receives pressure input but also exerts a reactive force on the gas. Since incompressible air cannot store energy via compression, the feedback occurs solely through velocity field adaptation, resulting in a pressure response that is out of phase with the fluid motion. This phase lag becomes more pronounced when the wave frequency approaches the membrane's natural frequency, as shown in Fig. 11(b). Nevertheless, this numerical phase lag has minimal impact on the predicted energy output, as energy conversion is controlled by capacitance variation induced by membrane deformation, which is independent of the air pressure phase.

It is worth noting that, in our previous study (Huang et al., 2025), no observable phase lag occurred between membrane deformation and air chamber pressure when the membrane was not pre-stretched. Due to the low stiffness in that case, the membrane

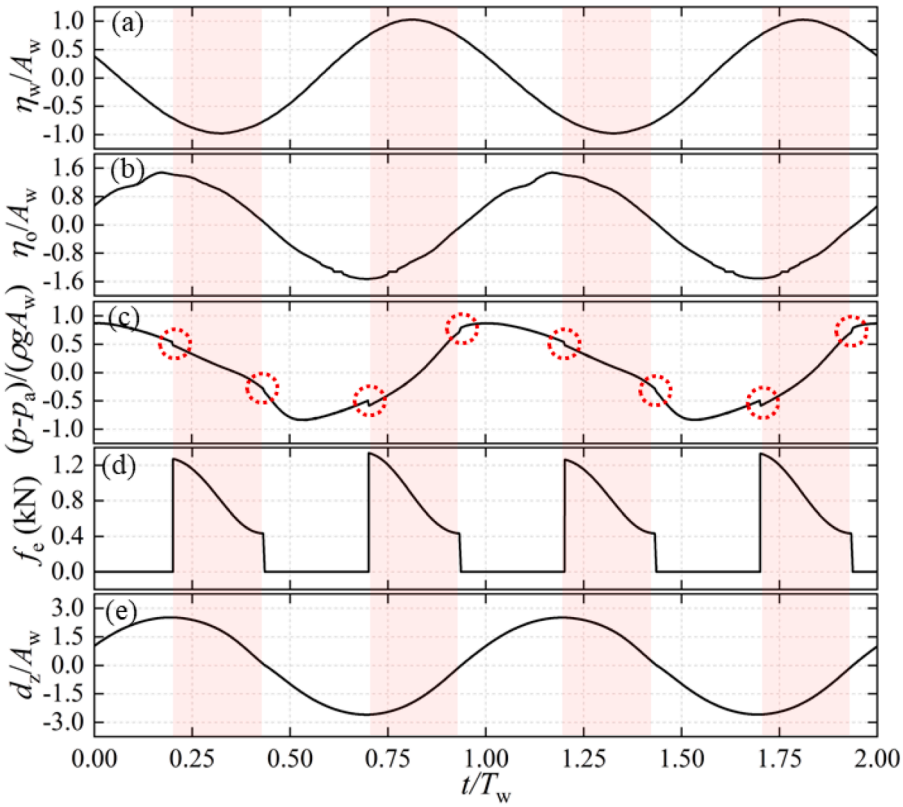

Fig. 10. Time history of key physical variables in load case LC2 at resonant frequency $f_w = 0.4$ Hz: (a) Normalized wave elevation η_w/A_w measured 1m in front of the OWC WEC; (b) Normalized free surface elevation η_o inside the OWC collector; (c) Normalized air chamber pressure $(p - p_a)/(\rho g A_w)$; (d) Electric force f_e acting on the DEG membrane; (e) Normalized vertical displacement at membrane centre d_z/A_w.

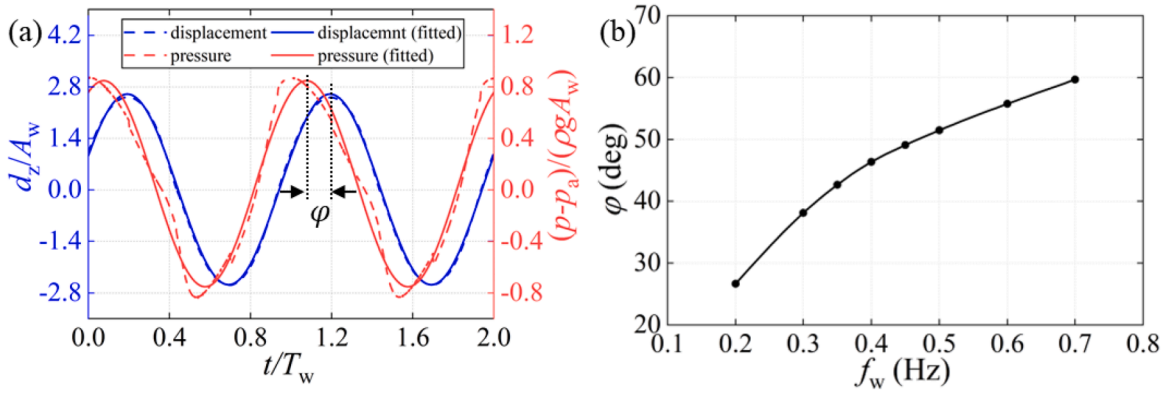

Fig. 11. Phase analysis in load case LC2 at resonant frequency $f_w = 0.4$ Hz: (a) Actual and fitted sinusoidal curves of normalized vertical displacement at membrane centre d_z/A_z and normalized air-chamber pressure $(p - p_a)/(\rho g A_w)$; (b) Phase difference φ between d_z and p as a function of wave frequency.

exerted negligible feedback on the internal air flow. As a result, the motion of the free surface, air pressure, and membrane displacement remained synchronized throughout the cycle. In contrast, the experimental study by Moretti et al. (Moretti et al., 2019) considered compressible air, where pressure variations followed the ideal gas law and were directly governed by changes in air chamber volume. Therefore, air pressure naturally remained in phase with the free surface motion, and consequently the phase lag did not appear in their results. The slight asymmetry observed in the pressure oscillations is attributed to the voltage-induced Maxwell stress, which modifies the effective stiffness of the membrane during upward and downward motion.

To further investigate the internal flow dynamics, the velocity and vorticity fields within the air chamber at different time instants over one wave period are visualized in Figs. 12 and 13. The black solid line in the figures denotes the air-water interface. A noticeable height difference exists between the internal and external free surfaces, which is the primary driver of the periodic pressure variation inside the air chamber. As expected, the instantaneous velocity distribution inside the air chamber is non-uniform, primarily due to the larger membrane deformation at the centre compared to the edges. This asymmetry pushes the air from the chamber centre toward the side walls. Consequently, a persistent downward flow is observed near the air-water interface at the centre, while upward flow occurs along the side walls. When the downward flow impinges on the air-water interface, it is deflected and forms a distinct vortex structure above the interface. Due to the relatively low air velocity, the vortex remains close to the interface and is not prominent in the upper region of the chamber. These complex flow features may influence the deformation modes of the DEG membrane. However, such behaviour cannot be captured by potential-flow-based reduced-order models (Moretti et al., 2019; Vertechy et al., 2013; Moretti et al., 2018; Rosati Papini et al., 2018).

5.2.2. *Structural dynamics*

To investigate the characteristics of membrane motion, Fig. 14 illustrates the membrane shape at different time instants, with colours representing the normalized vertical displacement (d_z/A_w). The results clearly show that the membrane deforms in an axisymmetric manner. Additionally, Fig. 15 presents the displacement contours along the membrane radius. For most of the time, the deformation predominantly exhibits a first-order mode. However, at specific time instants when the overall displacement is relatively small (e.g., $t = 0T_w$ and $t = 0.5T_w$ in Fig. 15b), a second-order mode emerges. This mode transition between first- and second-order modes reflects the realistic dynamic behaviour of the membrane, which is typically neglected and cannot be captured using reduced-order models (Moretti et al., 2019; Vertechy et al., 2013; Moretti et al., 2018; Rosati Papini et al., 2018).

Fig. 16 shows the von Mises stress distribution on the membrane, which exhibit a clear axisymmetric pattern. The von Mises stress is employed to represent the equivalent stress combines both normal and shear components within the membrane material. In addition, the instantaneous maximum stress consistently occurs either at the centre ($x/D = 0$) or at the edge ($x/D = 0.5$) of the membrane. Notably, a faint square-shaped pattern is visible near the centre of the membrane. This is a mesh-induced numerical effect arising from the structured mesh (see Fig. 7(d)) used for the membrane discretisation. The mesh contains a rectangular element cluster in the central region, which becomes visible when the deformation is small but does not affect the physical symmetry or the overall stress distribution.

To better illustrate this behaviour, Fig. 17(a) presents the spatial-temporal evolution of stress along the membrane radius. When the membrane exhibits a second-order deformation mode ($t = 0\ T_w$), the stress decreases monotonically from the centre toward the edge. In contrast, during a first-order deformation ($t = 0.5\ T_w$), the stress first decreases and then increases along the radial direction, reflecting the modal-dependent stress distribution.

Fig. 17(b) further shows that the largest stress variation occurs at membrane's edge ($x/D = 0.5$), followed by centre ($/D = 0$), indicating that both the centre and edge regions are subjected to the highest fatigue loading. These regions may therefore be more susceptible to mechanical failure and should be considered critical in reliability assessments.

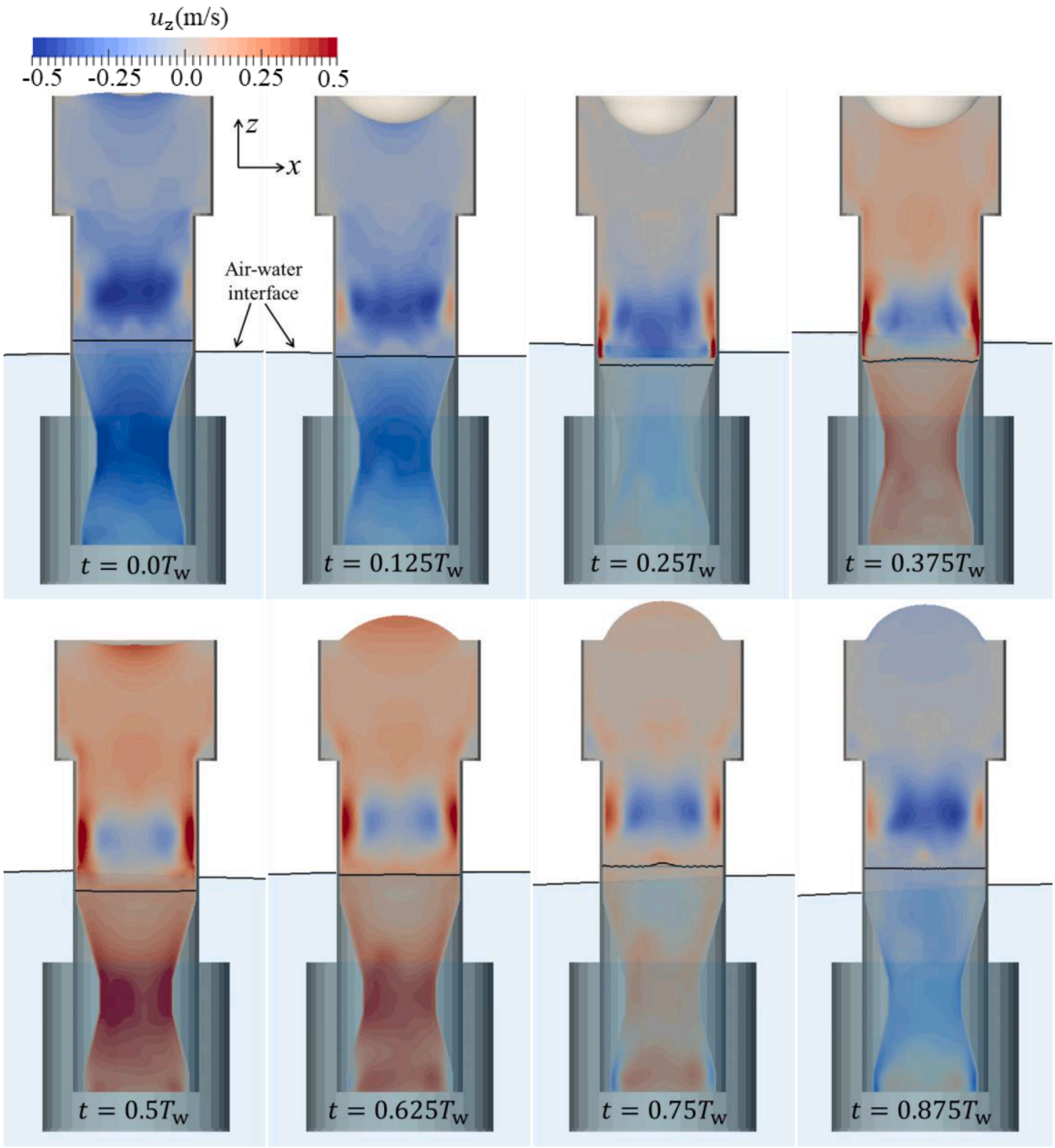

Fig. 12. Velocity field in the *x*-*z* plane at selected time instants over one wave period in load case LC2 at resonant frequency $f_w = 0.4$ Hz.

5.2.3. *Electrical characteristics*

As introduced in Section 4.2, the DEG membrane contributes to energy generation only during the capacitance-decreasing phase. Accordingly, the control circuit applies voltage to the membrane only during the half-cycle in which the membrane returns from its maximum deformation to the equilibrium position, as illustrated in Fig. 18(a). As a result, electrical energy is generated only during this half-cycle. Additionally, the applied voltage increases progressively as the membrane deformation decreases, following the designed control strategy. The power output shown in Fig. 18(b) illustrates that the peak power does not occur when the membrane reaches its maximum or minimum deformation but at an intermediate position, with a maximum of 0.59 W at model scale.

5.3. *Influence of electric field under different wave frequencies*

The electric field influences the OWC WEC system primarily by reducing the stiffness of membrane and thus increasing overall system damping. Studies on the electric impact are conducted at variable wave frequency with and without electric field, and the

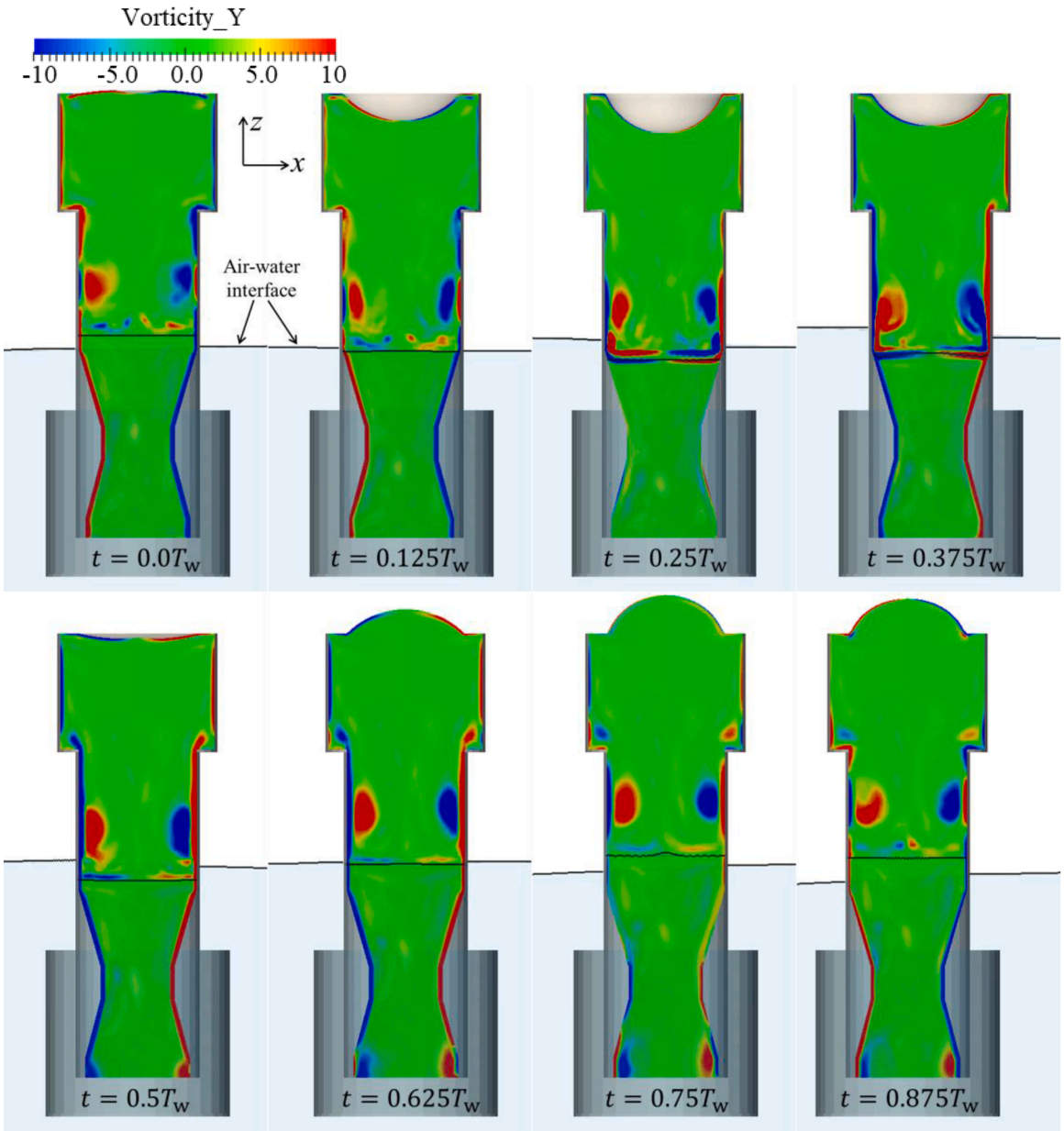

Fig. 13. Vorticity field in the x-z plane at selected time instants over one wave period in load case LC2 at resonant frequency $f_w = 0.4$ Hz.

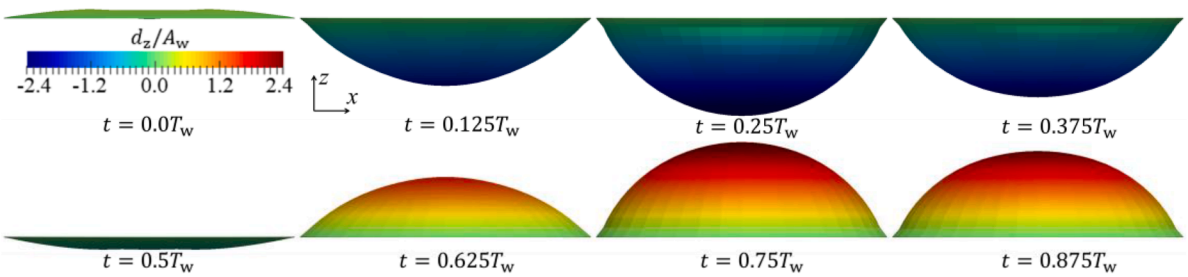

Fig. 14. Normalized vertical displacement d_z/A_w of the DEG membrane at selected time instants over one wave period in load case LC2 at resonant frequency $f_w = 0.4$ Hz).

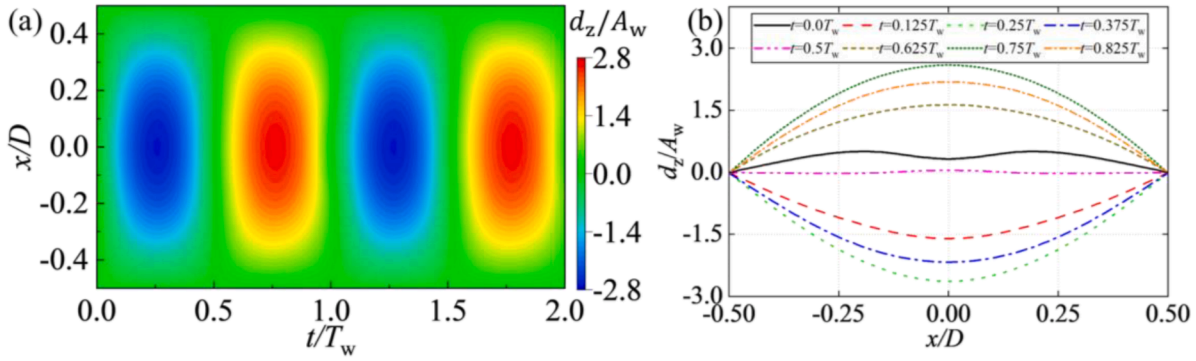

Fig. 15. Normalized vertical displacement (d_z/A_w) of the DEG membrane along the radial direction in load case LC2 at resonant frequency $f_w = 0.4$ Hz: (a) Spatial-temporal distribution of d_z/A_w; (b) Deformation profiles at selected time instants within one wave period.

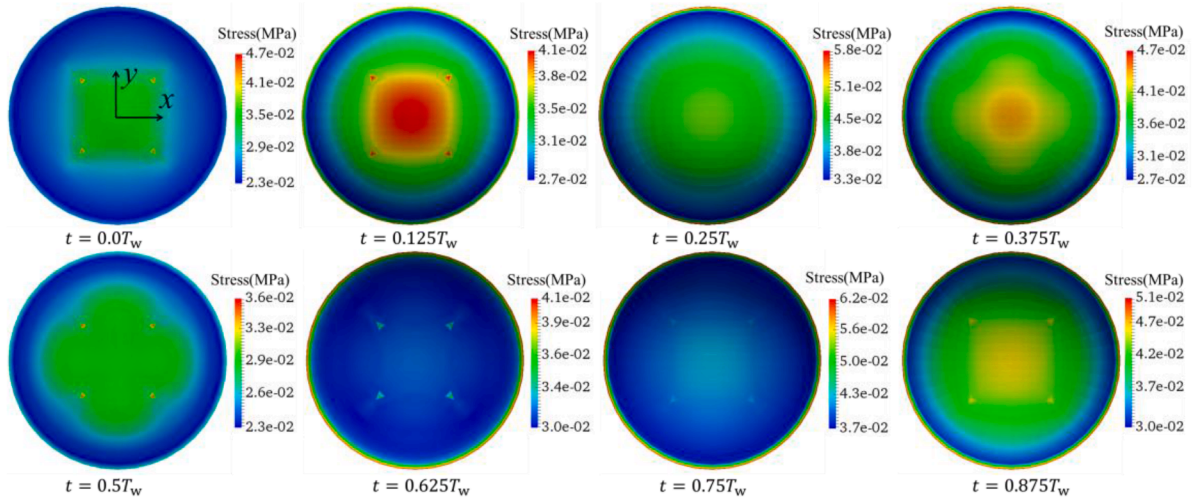

Fig. 16. Distribution of von Mises stress on the membrane surface at selected time instants over one wave period in load case LC2 at resonant frequency $f_w = 0.4$ Hz.

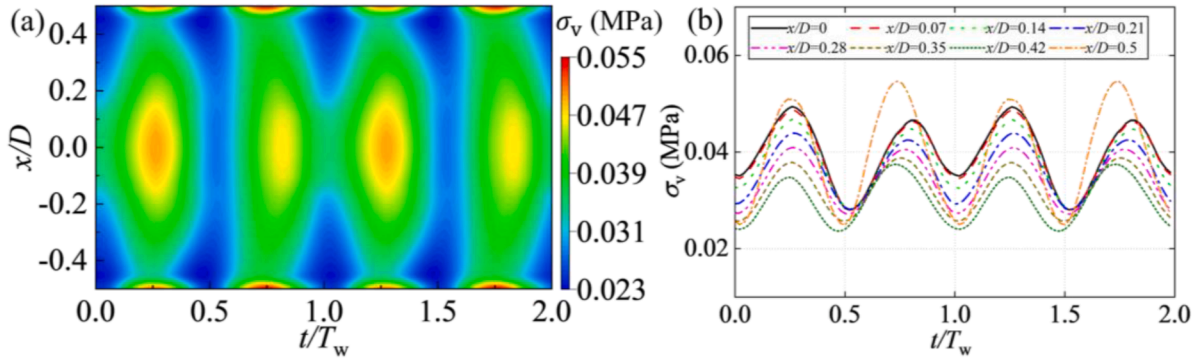

Fig. 17. Distribution of von Mises stress σ_v along the membrane radius in load case LC2 at resonant frequency $f_w = 0.4$ Hz: (a) Spatial-temporal distribution of σ_v; (b) Time histories of σ_v at different radial positions.

results are analysed in terms of the flow field, structural deformation, and power output.

5.3.1. *Flow field analysis*

Figs. 19–21 present the flow-related responses of the OWC WEC under various wave frequencies, with and without the inclusion of

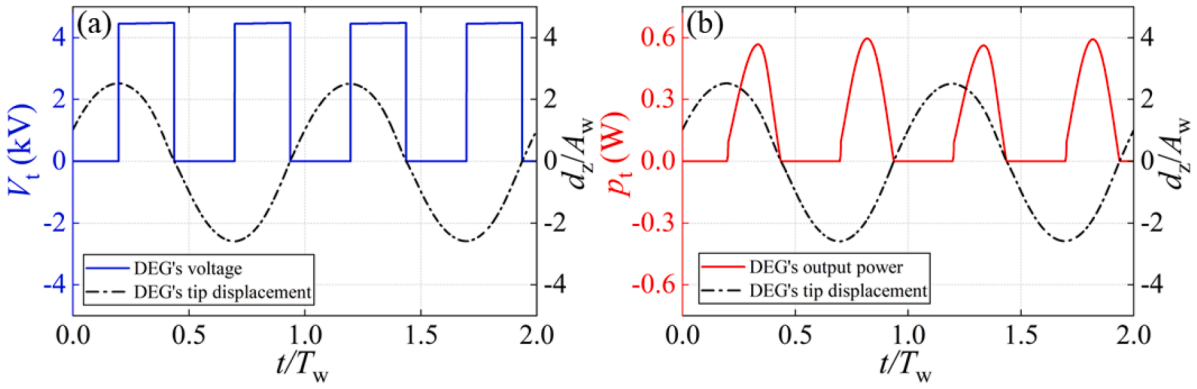

Fig. 18. Time histories of electrical variables in load case LC2 at resonant frequency $f_w = 0.4$ Hz: (a) Voltage V_t applied to the DEG membrane; (b) Instantaneous electrical power output p_t.

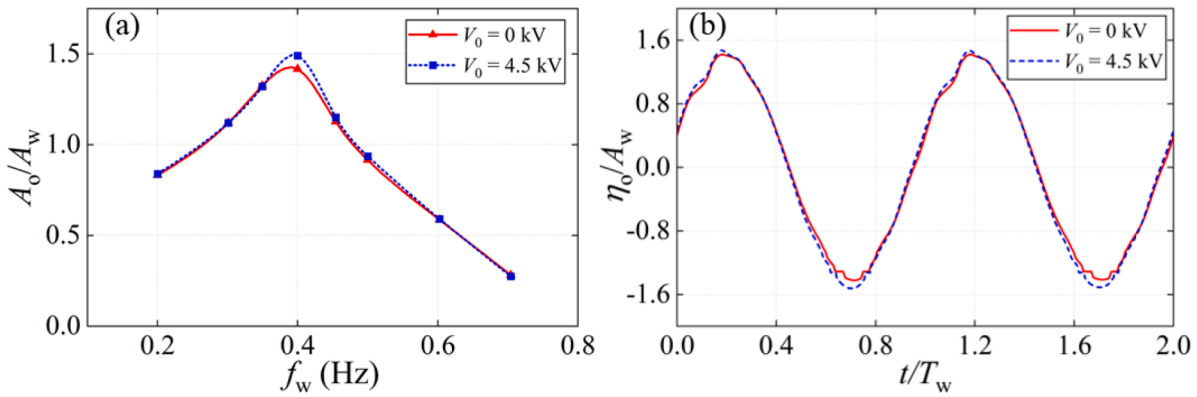

Fig. 19. OWC response with and without electric field in load cases LC1 and LC2: (a) Normalized OWC amplitude A_0/A_w under varying wave frequencies; (b) Time history of normalized free surface elevation η_0/A_w at resonant frequency $f_w = 0.4$ Hz.

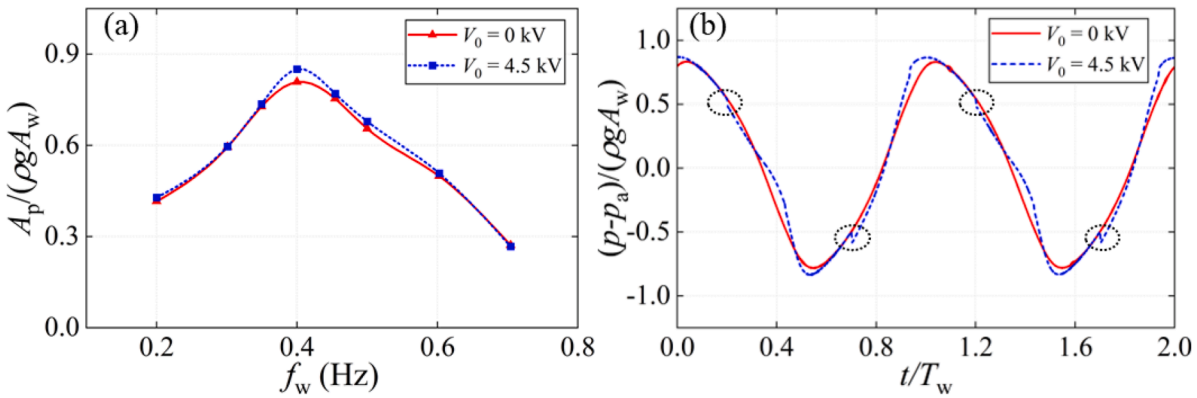

Fig. 20. Pressure response in the air chamber for load cases LC1 and LC2: (a) Pressure amplitude A_p normalized by the hydrostatic pressure $\rho g A_w$ under different wave frequencies; (b) Time history of air pressure at resonant frequency $f_w = 0.4$ Hz.

an electric field ($V_0 = 4.5$ kV and $V_0 = 0$ kV, respectively). The comparisons include the OWC amplitude (A_o), the pressure amplitude inside the air chamber (A_p), and the vertical displacement amplitude at membrane centre (A_d).

The results show that the applied electric field does not significantly alter the system's resonant frequency. In both cases, the maximum A_o, A_p, and A_d occur at f_w =0.4 Hz. However, the electric field reduces the membrane's effective stiffness, as indicated by the abrupt pressure change when the electric field is switched on or off (see black circles in Fig. 20(b)). This sudden variation is attributed to stiffness shifts induced by the electric actuation.

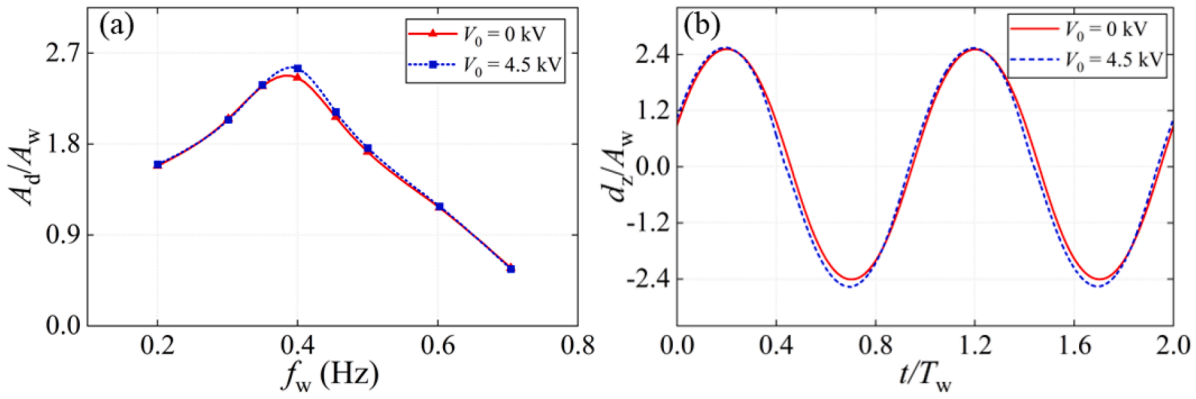

Fig. 21. Displacement response of the DEG membrane in load cases LC1 and LC2: (a) Normalized vertical displacement amplitude at membrane centre A_d/A_w; (b) Time history of normalized vertical displacement at the membrane centre d_z/A_w at resonant frequency $f_w = 0.4$ Hz.

Since the electric force is proportional to membrane deformation, its impact becomes more pronounced near resonance (i.e., within $f_w = 0.35 \sim 0.45$ Hz), where deformation is larger. Under these conditions, the application of the electric field leads to noticeable increases in A_o, A_p, and A_d, by approximately 5.1%, 5.3%, and 3.8%, respectively. In contrast, away from resonance, the influence of the electric field becomes negligible, with nearly identical values of A_o, A_p, and A_d for both $V_0 = 0$ and 4.5 kV.

To further examine the influence of the electric field on the internal flow, Fig. 22 presents the velocity and vorticity fields in the *x*-*z* plane for the OWC WEC at resonance frequency ($f_w = 0.4$ Hz) without electric actuation ($V_0 = 0$ kV). A comparison with the case involving an applied electric field ($V_0 = 4.5$ kV; see Figs. 12 and 13) reveals that the electric field has a limited impact on the overall flow pattern. Similar to the electrically actuated case, a persistent downward flow appears near the free surface at the centre of the air chamber, giving rise to a distinct vortex in that region.

5.3.2. *Structural responses*

We first examine the influence of the electric field on membrane deformation at the resonant frequency ($f_w = 0.4$ Hz). Fig. 23 shows the spatial-temporal distribution of membrane displacement along the membrane radius without the electric field ($V_0 = 0$ kV). Compared to the case with electric field ($V_0 = 4.5$ kV; see Fig. 15(b)), both scenarios predominantly exhibit a first-order deformation mode when the membrane displacement is large. However, with the electric field applied, the second-order mode becomes more pronounced as the membrane approaches a flat configuration.

To further investigate this behaviour, Fig. 24 presents the membrane deformation under various wave frequencies at the instant when the membrane centre displacement is zero. In both cases, with and without the electric field, the prominence of the second-order mode increases as the deformation amplitude grows. Notably, the electric field amplifies this effect, suggesting that it facilitates the excitation of higher-order deformation modes, resulting in more complex membrane behaviour.

The effect of the electric field on membrane stress is also analysed at resonance. Fig. 25 shows the spatial-temporal stress distribution along the radius direction for the case without the electric field. Compared with the case with the electric field applied ($V_0 = 4.5$ kV; see Fig. 17), the electric field does not significantly alter the overall stress pattern or the locations of maximum stress. In both cases, the maximum stress and its largest variation occur at the membrane edge (x/D = 0.5), followed by the centre (x/D = 0).

However, as shown in Fig. 26, the electric field increases the overall stress level. Specifically, under $V_0 = 4.5$ kV, the maximum stress and its amplitude at the membrane edge increase by 3.2% and 5.7%, respectively, while at the centre, the increases reach 8.8% and 28%. This indicates that the electric field significantly amplifies fatigue loading at both critical locations, potentially increasing the risk of structure failure.

Furthermore, Fig. 27 illustrates the electric field's influence on membrane stress at the centre and edge across different wave frequencies. In all cases, the electric field increases both the maximum stress and stress variation at these locations, with a more substantial effect observed at the centre. The magnitude of this effect also correlates positively with the deformation amplitude.

5.3.3. *Electrical output*

As previously discussed, the electric field is applied only during the phase when the membrane deformation decreases, during which the membrane capacitance reduces and the applied voltage from the control circuit gradually increases. Fig. 28(a) illustrates the voltage variation across the membrane at different wave frequencies. Since membrane capacitance is directly related to its deformation, the voltage range follows a similar trend to the membrane displacement across frequencies, both reaching a maximum at the resonant frequency ($f_w = 0.4$ Hz) and decreasing as the wave frequency deviates from resonance.

The electrical power output of the OWC WEC, including both average and maximum values, exhibits the same frequency dependence, as shown in Fig. 28(b). The maximum power ranges from 0.10 W to 0.59 W across the tested frequency range ($f_w = 0.2 \sim 0.6$ Hz).

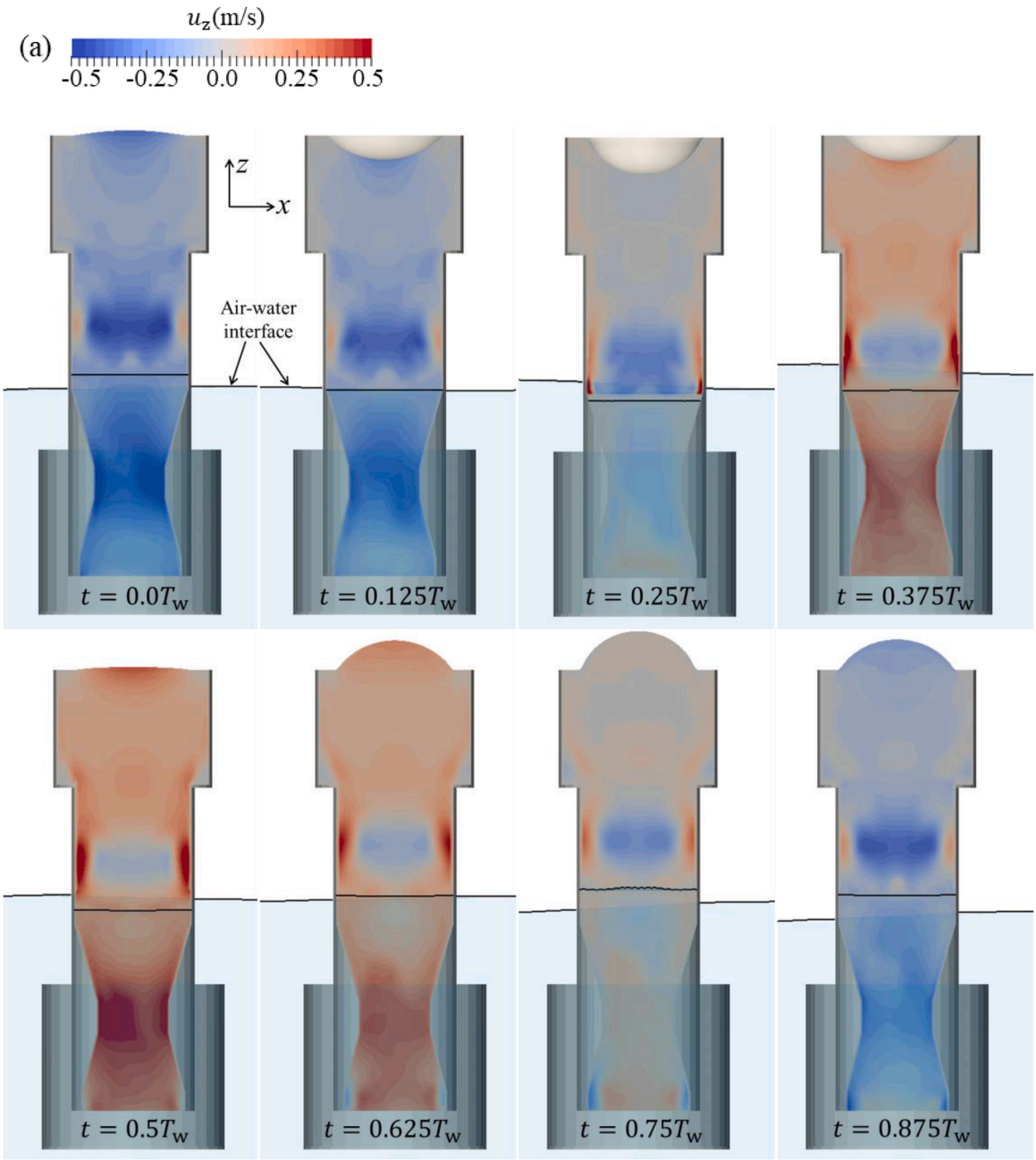

Fig. 22. Flow field in the *x*-*z* plane of air chamber at selected time instants over one wave period in load case LC1 at resonant frequency $f_w = 0.4$ Hz: (a) Velocity field; (b) Vorticity distribution.

5.4. Influence of voltage magnitude at resonant frequency

The applied voltage directly affects the electric field intensity acting on the DEG membrane, thereby altering its mechanical response. To examine this effect, a series of simulations were performed at a resonant wave frequency ($f_w = 0.4$ Hz) under different initial voltages (V_0) ranging from 1.5 kV to 4.5 kV. The effects of voltage magnitude on the flow field, structural response, and power output were systematically analysed.

5.4.1. Flow field analysis

As shown in Fig. 29, increasing the initial voltage (V_0) enhances the electric field intensity acting on the DEG membrane, thereby

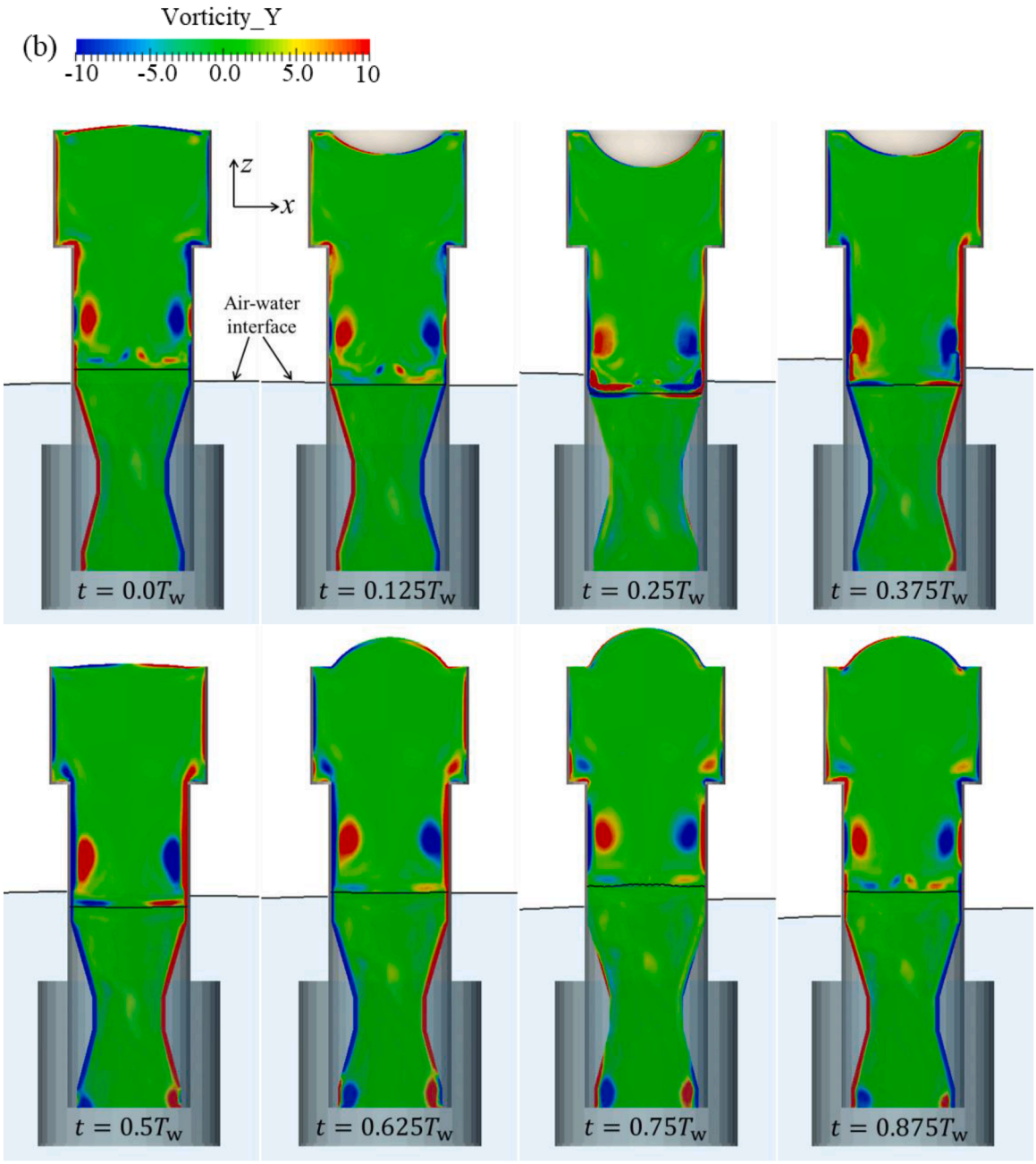

Fig. 22. (*continued*).

increasing the resulting electrostatic force (f_e). This leads to a reduction in the membrane's effective stiffness and, consequently, an increase in its deformation amplitude (A_d). The enhanced membrane motion further amplifies the oscillation amplitude of the OWC (A_o) and the pressure variation in the air chamber (A_p). Notably, these variables do not increase linearly with voltage. Instead, a near-quadratic relationship is observed, indicating that both membrane deformation and air-chamber pressure are highly sensitive to changes in voltage magnitude.

5.4.2. Structural responses

The influence of voltage on membrane deformation is most evident when the membrane approaches the flat configuration. As shown in Fig. 30(a), higher voltages lead to more pronounced second-order deformation modes, indicating that increased electric field intensity tends to excite higher-order membrane responses.

Fig. 30(b) presents the maximum stress distributions along the membrane radius under different voltage levels. Increasing the

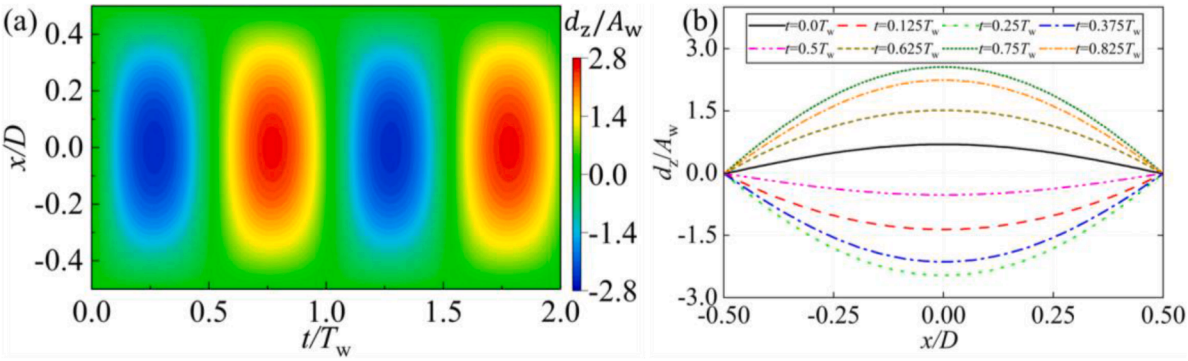

Fig. 23. Deformation of the DEG membrane along the radial direction in load case LC1 at resonant frequency $f_w = 0.4$ Hz: (a) Spatial-temporal distribution of normalized displacement d_z/A_w; (b) Deformation profiles at selected time instants.

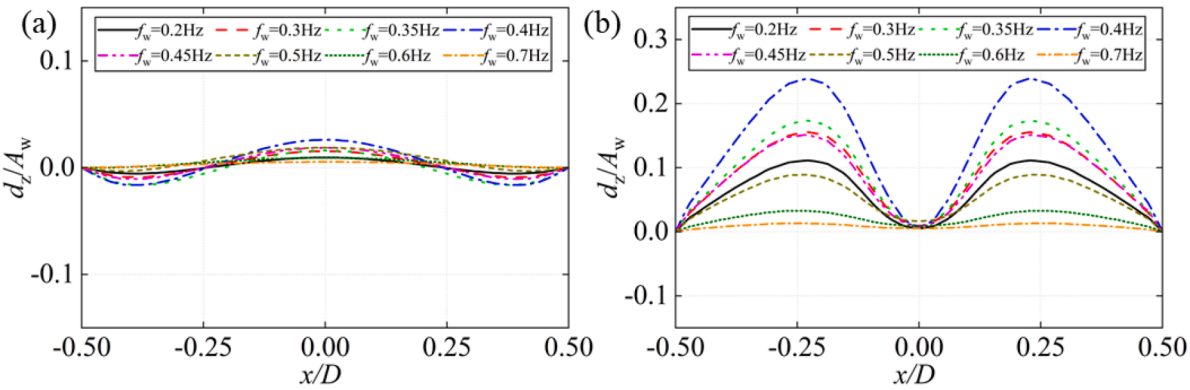

Fig. 24. Membrane deformation near the flat configuration under different wave frequencies in load cases LC1 and LC2: (a) Without electric field ($V_0 = 0$ kV); (b) With electric field ($V_0 = 4.5$ kV).

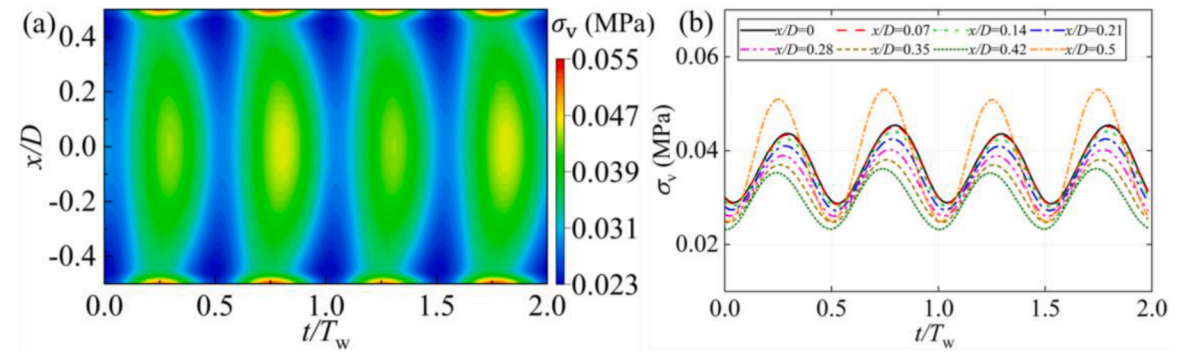

Fig. 25. Distribution of von Mises stress σ_v along the membrane radius in load case LC1 at resonant frequency $f_w = 0.4$ Hz: (a) Spatial-temporal distribution; (b) Time histories of σ_v at different radial positions.

voltage significantly raises the stress at the membrane centre, while the effect at the edge remains limited. As illustrated in Fig. 31, when the applied voltage increases from 1.5 kV to 4.5 kV, the maximum stress and stress variation at the centre rise by 8.2% and 24%, respectively, compared to only 1.9% and 3.2% at the edge. These results indicate that the membrane centre is more sensitive to electric field intensity.

5.4.3. Electrical output

As previously noted, an increase in the initial voltage leads to greater membrane deformation, which in turn results in a larger voltage variation across the membrane, as shown in Fig. 32(a). The increased deformation also amplifies the variation in membrane

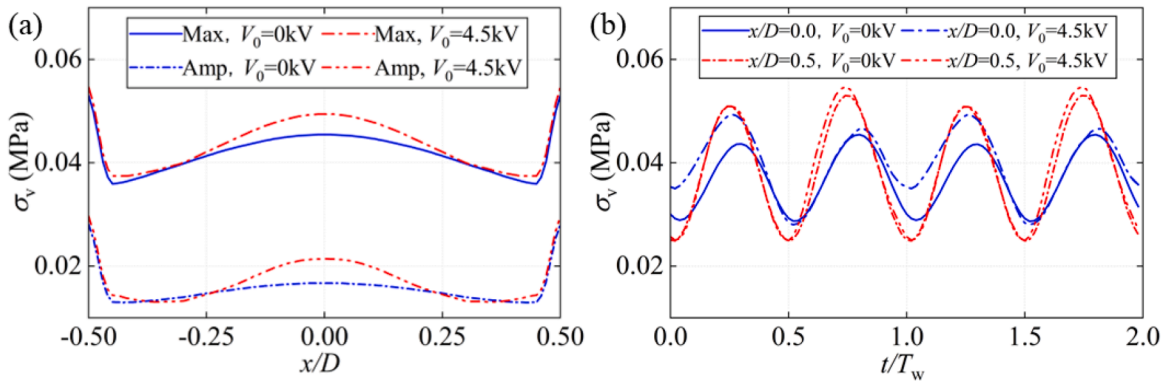

Fig. 26. Comparison of membrane stress with and without the electric field in load cases LC1 and LC2 at resonant frequency $f_w = 0.4$ Hz: (a) Maximum von Mises stress σ_v and its variation amplitude; (b) Time histories of von Mises stress σ_v at the membrane centre and edge.

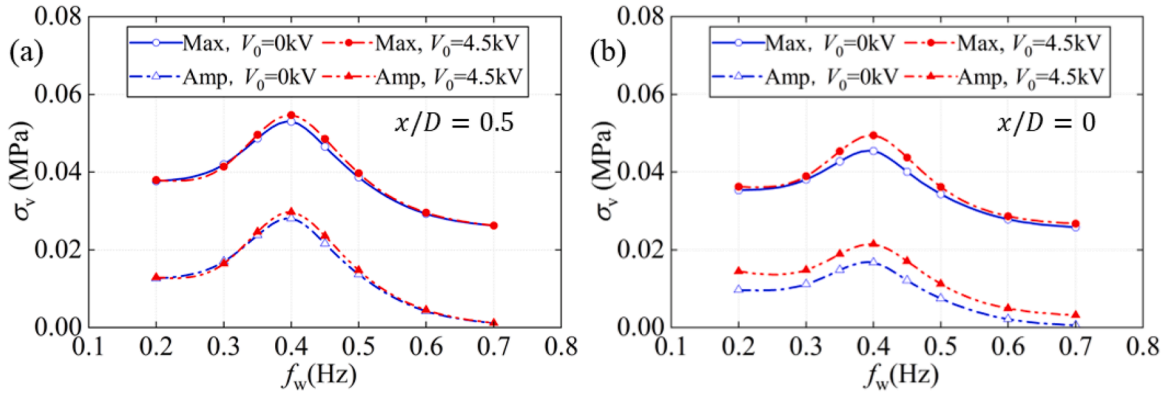

Fig. 27. Influence of the electric field on membrane stresses under different wave frequencies f_w in load cases LC1 and LC2: (a) Von Mises stress σ_v at membrane edge ($x/D = 0.5$); (b) Von Mises stress σ_v at membrane centre ($x/D = 0$).

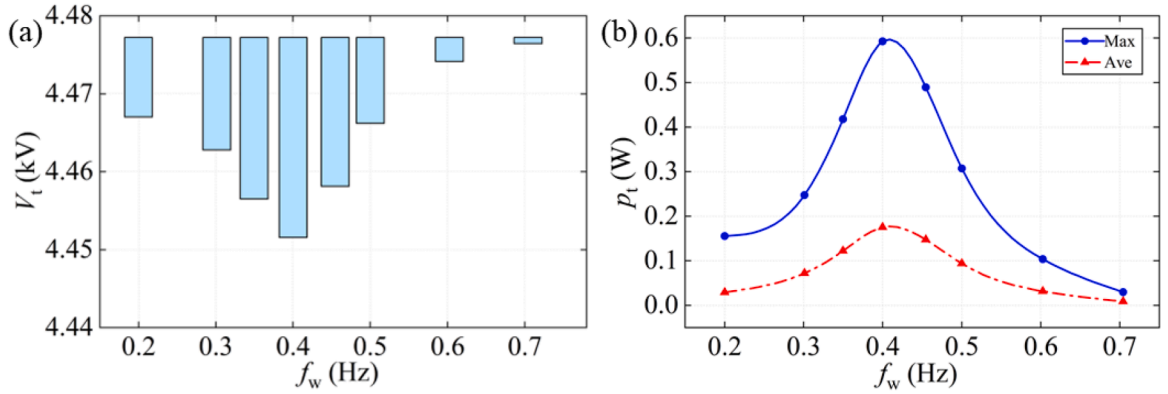

Fig. 28. Electrical performance of the OWC WEC under different wave frequencies f_w in load case LC2: (a) Variation range of membrane voltage V_t; (b) Average and maximum electrical power output p_t.

capacitance, thereby enhancing the electrical energy output. However, it is important to note that the membrane has a material-dependent breakdown voltage. Therefore, the output power cannot be increased indefinitely by simply raising the applied voltage. Additionally, dielectric elastomer membranes are also susceptible to dielectric fatigue under prolonged cyclic electromechanical loading, which may gradually reduce their breakdown strength and actuation capability. Therefore, in practical design, an optimal operating voltage should be identified to balance energy conversion efficiency and long-term durability.

As illustrated in Fig. 32(b), the electrical output power increases with applied voltage in a nonlinear, approximately quadratic

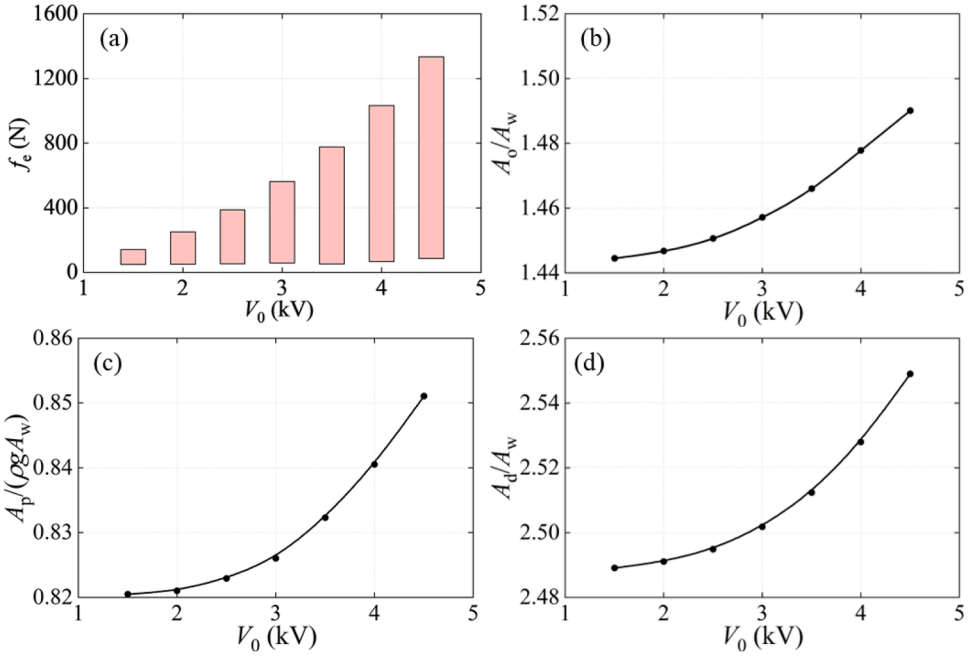

Fig. 29. Variation of key response variables with the initial voltage V_0 in load case LC3: (a) Electric force f_e acting on the membrane; (b) Response amplitude operator A_0/A_w of the OWC chamber; (c) pressure amplitude A_p in the air chamber, normalized by static pressure $\rho g A_w$; (d) Normalized vertical displacement amplitude at membrane centre A_d/A_w.

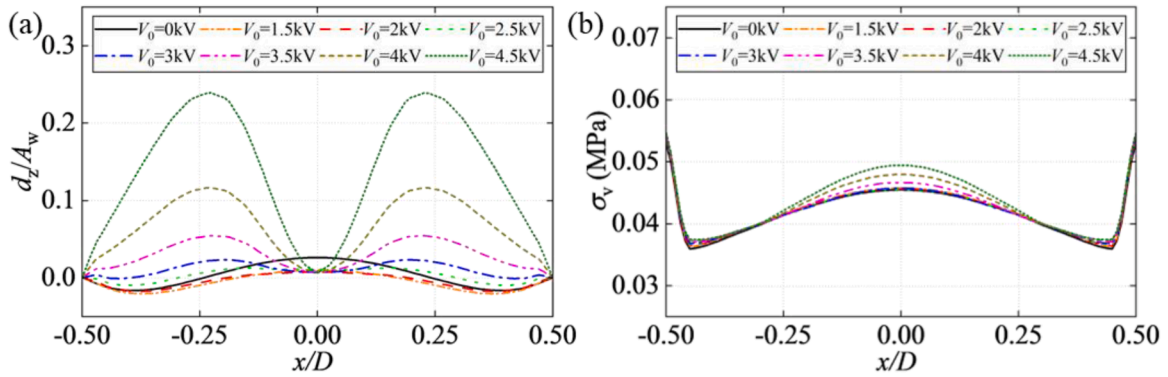

Fig. 30. Structural responses of the DEG membrane under different initial voltages V_0 in load case LC3: (a) Normalized membrane displacement d_z/A_w near the flat configuration; (b) Maximum von Mises stress σ_v along the membrane diameter.

manner. The maximum power increases from 0.06 W to 0.59 W as the initial voltage rises from 1.5 kV to 4.5 kV, demonstrating the voltage-dependent enhancement of energy conversion performance.

6. Conclusions

In this study, a high-fidelity multiphysics analysis framework was developed based on CFD, FEA, and parallel-plate capacitor theory. This framework is designed to simulate the interaction among fluid, flexible structures, and electric fields in a DEG-integrated OWC WEC. A two-way strong coupling strategy is used to accurately capture the dynamic response of the system. The framework was first validated using experimental results from an electrically driven membrane deformation test. We then applied this framework to investigate the behaviour of the flexible OWC WEC under different wave frequencies, with and without electric field activation, and for varying applied voltages.

The results show that applying an electric field reduces the membrane's stiffness. At the resonance conditions, the membrane deformation amplitude increased by 3.8% when the electric field was applied. However, the resonance frequency remained nearly unchanged. Due to the control circuit design, the electric field only acts when the membrane is contracting, and its capacitance is

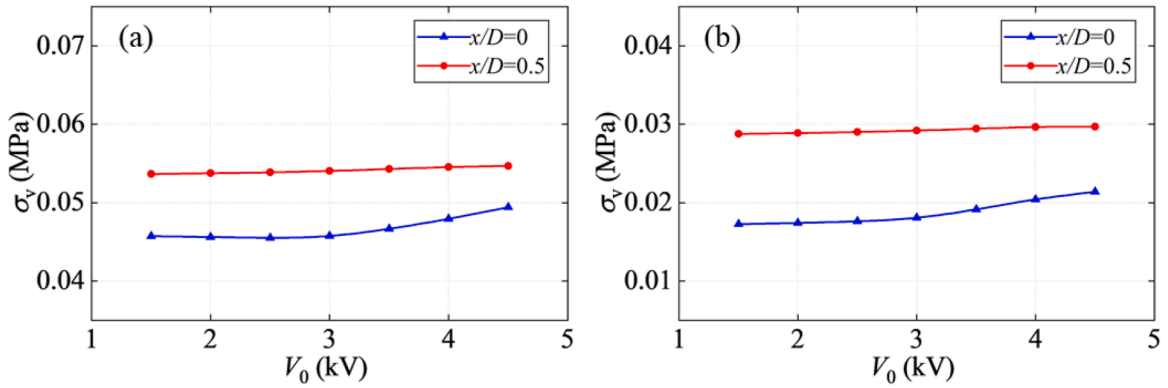

Fig. 31. Membrane stress σ_v at centre (blue line) and edge (red line) under various voltage magnitudes V_0 in load case LC3: (a) Maximum von Mises stress; (b) Stress variation amplitude.

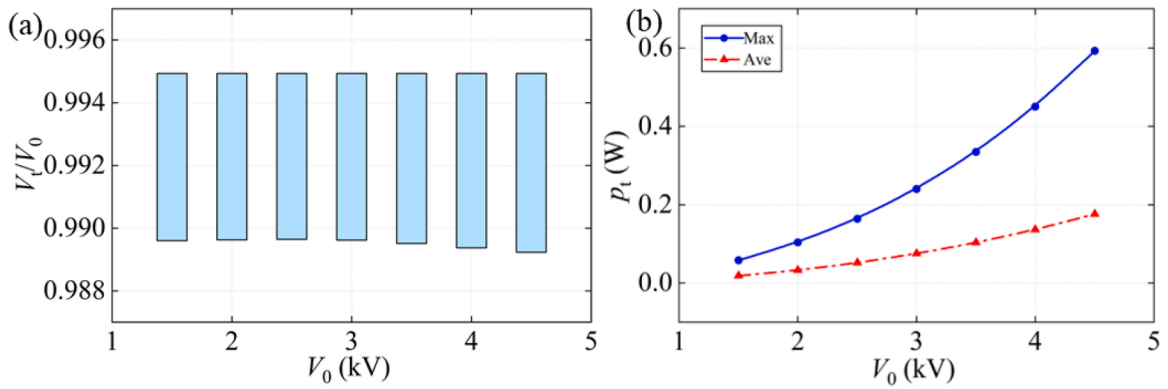

Fig. 32. Electrical output of the OWC WEC under different initial voltages V_0 in load case LC3: (a) Variation of normalized membrane voltage V_t/V_0; (b) Average and maximum electrical power output p_t.

decreasing. This leads to the abrupt changes in membrane stiffness during charging and discharging, which causes pressure spikes in the air chamber.

The internal flow field is less sensitive to the electric field. Regardless of whether the electric field is applied, a persistent downward velocity region and stable vortex structure form near the lower part of the air chamber close to the free surface. In contrast, the membrane's structural response becomes more complex when the electric field is active. Near the flat configuration, the membrane exhibits stronger second-order deformation modes, which become more pronounced with higher voltage. At large deformations, however, the response is still dominated by the first-order mode.

The electric field also increases the overall membrane stress, especially at the centre and edge. For an initial voltage of 4.5 kV, the maximum stress and stress variation at the membrane centre increase by 8.8% and 28%, respectively, compared to the case without electric field activation, while the corresponding increases at the edge are 3.2% and 5.7%. These areas are the most critical for stress concentration, regardless of whether an electric field is present, and require special attention to fatigue failure risks.

As the initial voltage increases, the electric force, membrane deformation, stress level, and output power all increase. These quantities follow a quadratic growth trend. When the voltage is raised from 1.5 kV to 4.5 kV, the maximum output power increases from 0.06 W to 0.59 W, indicating strong potential of the DEG-integrated OWC concept for practical wave energy applications.

Overall, this work advances the understanding of the fluid-structure-electricity coupling mechanisms in flexible OWC WECs and elucidates the role of electric field parameters in shaping the dynamic and energy performance of the device. The findings provide valuable insights for the optimization of device design and the enhancement of energy output. Moreover, the proposed multiphysics framework is readily extendable to other complex coupling scenarios, offering a versatile tool for future investigations. It should be noted, however, that air compressibility is not considered in the present model. Although this simplification does not significantly affect the conclusions drawn in this study, it introduces a deviation from real physical conditions. Future work will aim to incorporate air compressibility effects and apply the model to the analysis of flexible tube-type WECs to further broaden its applicability.

CRediT authorship contribution statement

Yang Huang: Writing – review & editing, Writing – original draft, Visualization, Validation, Software, Methodology, Investigation,

Formal analysis, Data curation, Conceptualization. **Qing Xiao:** Writing – review & editing, Supervision, Resources, Project administration, Methodology, Investigation, Funding acquisition, Conceptualization. **Liu Yang:** Funding acquisition, Formal analysis, Conceptualization. **Saishuai Dai:** Methodology, Formal analysis, Conceptualization. **Saeid Lotfian:** Formal analysis, Conceptualization. **Feargal Brennan:** Funding acquisition, Conceptualization.

Declaration of competing interest

The authors declare that they have no known competing financial interests or personal relationships that could have appeared to influence the work reported in this paper.

Acknowledgements

This research was supported by an Engineering and Physical Sciences Research Council (EPSRC) Grant “Bionic Adaptive Stretchable Materials for WEC (BASM-WEC)” (EP/V040553/1). The authors gratefully acknowledge the support of the EPSRC High-End Computing Consortium for Wave Structure Interaction (HEC-WSI), under grant number EP/X035751/1, for providing access to ARCHER2 HPC resources.

Data availability

Data will be made available on request.

References

Hamedi, Z., Korban, R., Gonul, G., et al., 2018. Citation: IRENA (2018), renewable energy outlook: Egypt. Int. Renew. Energy Agency Abu Dhabi.
Aderinto, T., Li, H., 2018. Ocean wave energy converters: status and challenges. Energies 11 (5), 1250.
Collins, I., Hossain, M., Dettmer, W., et al., 2021. Flexible membrane structures for wave energy harvesting: a review of the developments, materials and computational modelling approaches. Renew. Sustain. Energy Rev. 151, 111478.
Vertechy R, Fontana M, Papini G P R, et al. In-tank tests of a dielectric elastomer generator for wave energy harvesting[C]//Electroactive Polymer Actuators and Devices (EAPAD) 2014. SPIE, 2014, 9056: 332-342.
Kornbluh, R D, Pelrine, R., Prahlad, H., et al., 2012. From boots to buoys: promises and challenges of dielectric elastomer energy harvesting. Electroact. Polym. Mater. 67–93.
Kaltseis, R., Keplinger, C., Koh, S J A, et al., 2014. Natural rubber for sustainable high-power electrical energy generation. Rsc Adv. 4 (53), 27905–27913.
Liu, Z., Zhang, R., Xiao, H., et al., 2020. Survey of the mechanisms of power take-off (PTO) devices of wave energy converters. Acta Mech. Sin. 36, 644–658.
Suo, Z., 2010. Theory of dielectric elastomers. Acta Mech. Solida Sin. 23 (6), 549–578.
Pelrine, R., Kornbluh, R D, Eckerle, J., et al., 2001. Dielectric elastomers: generator mode fundamentals and applications[C]. //. In: Smart Structures and Materials 2001: Electroactive Polymer Actuators and Devices, 4329. SPIE, pp. 148–156.
Peatfield, A M, Bellamy, N W, Duckers, L J, et al., 1987. Wave energy: a british way forward with the circular sea clam[C]. //. In: IEE Conference Publication. IEEE, pp. 194–197.
AWS, 2025. AWS-III Multi-Cell Wave Power Generator. https://www.awsocean.com/multi-cell-wave-power/ [Accessed 14 July 2025].
Orphin, J., Fleming, A., Algie, C., 2017. Physical scale model testing of a flexible membrane wave energy converter: videogrammetric analysis of membrane operation. Int. J. Mar. Energy 20, 135–150.
Fontana, M., Daniele, L., Moretti, G., et al., 2018. Wave Motion Generator Based On A Dielectric Elastomer With Stiffness Compensation. WO Patent, 116276.
Moretti, G., Forehand, D., Vertechy, R., et al., 2014. Modeling of an oscillating wave surge converter with dielectric elastomer power take-off[C]. //. In: International Conference on Offshore Mechanics and Arctic Engineering. American Society of Mechanical Engineers, 45530. V09AT09A034.
Moretti, G., Rosati Papini, G P, Daniele, L., et al., 2019. Modelling and testing of a wave energy converter based on dielectric elastomer generators. Proc. R. Soc. A 475 (2222), 20180566.
Moretti, G., Malara, G., Scialò, A., et al., 2020. Modelling and field testing of a breakwater-integrated U-OWC wave energy converter with dielectric elastomer generator. Renew. Energy 146, 628–642.
Symphony Wave Power, How Does It Work?, 2025. https://symphonywavepower.com/how-does-it-work/ [Accessed 14 July 2025].
Vertechy, R., Fontana, M., Papini, G P R, et al., 2013. Oscillating-water-column wave-energy-converter based on dielectric elastomer generator[C]. //. In: Electroactive Polymer Actuators and Devices (EAPAD) 2013, 8687. SPIE, pp. 130–142.
Rosati Papini, G P, Vertechy, R., Fontana, M., 2013. Dynamic model of dielectric elastomer diaphragm generators for oscillating water column wave energy converters [C]. //. In: Smart Materials, Adaptive Structures and Intelligent Systems, 56031. American Society of Mechanical Engineers. V001T03A038.
Falcão, A F O, Henriques, J C C, 2016. Oscillating-water-column wave energy converters and air turbines: a review. Renew. Energy 85, 1391–1424.
Rosati Papini, G P, Vertechy, R., Fontana, M., 2013. Dynamic model of dielectric elastomer diaphragm generators for oscillating water column wave energy converters [C]. // Smart Materials, Adaptive Structures and Intelligent Systems. American Society of Mechanical Engineers, 56031. V001T03A038.
Moretti, G., Rosati, G P P, Alves, M., et al., 2015. Analysis and design of an oscillating water column wave energy converter with dielectric elastomer power take-off [C]. //. In: International Conference on Offshore Mechanics and Arctic Engineering, 56574. American Society of Mechanical Engineers. V009T09A023.
Moretti, G., Papini, G P R, Righi, M., et al., 2018. Resonant wave energy harvester based on dielectric elastomer generator. Smart Mater. Struct. 27 (3), 035015.
Rosati Papini, G P, Moretti, G., Vertechy, R., et al., 2018. Control of an oscillating water column wave energy converter based on dielectric elastomer generator. Nonlinear Dyn. 92, 181–202.
Moretti, G., Malara, G., Scialò, A., et al., 2020. Modelling and field testing of a breakwater-integrated U-OWC wave energy converter with dielectric elastomer generator. Renew. Energy 146, 628–642.
Abad, F., Lotfian, S., Dai, S., et al., 2024. Experimental and computational analysis of elastomer membranes used in oscillating water column WECs. Renew. Energy 226, 120422.
Schumacher, C., Marschner, S., Gross, M., et al., 2018. Mechanical characterization of structured sheet materials. ACM Trans. Graph. (TOG) 37 (4), 1–15.
Wang, F., Yuan, C., Lu, T., et al., 2017. Anomalous bulging behaviors of a dielectric elastomer balloon under internal pressure and electric actuation. J. Mech. Phys. Solids 102, 1–16.
Huang, Y., Idarraga, G., Abad, F., et al., 2025. Oscillating water column wave energy converter with flexible structured sheet material for enhanced power output. Energy Convers. Manag. 333, 119794.
Huang, Y., Xiao, Q., Idarraga, G., et al., 2023. Novel computational fluid dynamics-finite element analysis solution for the study of flexible material wave energy converters. Phys. Fluids 35 (8).

Huang, Y., Xiao, Q., Idarraga, G., et al., 2025. Bio-inspired adaptive flexible tube wave energy converters: resonant fluid-structure interaction and power extraction. Phys. Fluids 37 (5).
Smagorinsky, J., 1963. General circulation experiments with the primitive equations: I. The basic experiment. Mon. Weather Rev. 91 (3), 99–164.
Deardorff, J W, 1970. A numerical study of three-dimensional turbulent channel flow at large Reynolds numbers. J. Fluid Mech. 41 (2), 453–480.
Christensen, E D, Deigaard, R., 2001. Large eddy simulation of breaking waves. Coast. Eng. 42 (1), 53–86.
Higuera, P., Lara, J.L., Losada, I.J., 2014. Three-dimensional interaction of waves and porous coastal structures using OpenFOAM®. Part I: formulation and validation. Coast. Eng. 83, 243–258.
Higuera, P., Lara, J.L., Losada, I.J., 2014. Three-dimensional interaction of waves and porous coastal structures using OpenFOAM®. Part II: application. Coast. Eng. 83, 259–270.
Mooney, M., 1940. A theory of large elastic deformation. J. Appl. Phys. 11 (9), 582–592.
Newmark, N M, 1959. A method of computation for structural dynamics. J. Eng. Mech. Div. 85 (3), 67–94.
Yan, F N, Wong, H K, 1993. Force between the plates of a parallel-plate capacitor. Am. J. Phys. 61 (12), 1153. -1153.
Jasak, H., Jemcov, A., Tukovic, Z., 2007. OpenFOAM: a C++ library for complex physics simulations[C]. //. In: International Workshop On Coupled Methods In Numerical Dynamics, 1000, pp. 1–20.
Dhondt G. Calculix Crunchix User's Manual Version 2.12. Munich, Germany, accessed Sept, 2017, 21: 2017.
Degroote, J., Bathe, K J, Vierendeels, J., 2009. Performance of a new partitioned procedure versus a monolithic procedure in fluid–structure interaction. Comput. Struct. 87 (11-12), 793–801.
Lindner F, Mehl M, Uekermann B. Radial basis function interpolation for black-box multi-physics simulations. 2017.
Fox, J W, Goulbourne, N C, 2008. On the dynamic electromechanical loading of dielectric elastomer membranes. J. Mech. Phys. Solids 56 (8), 2669–2686.
Boccotti, P., 2003. On a new wave energy absorber. Ocean Eng. 30 (9), 1191–1200.
Liu, Z., Xu, C., Kim, K., et al., 2024. Hydrodynamic and energy-harvesting performance of an isolated oscillating water column device: an experimental study. Coast. Eng. 189, 104459.
Jiang, L., Betts, A., Kennedy, D., Jerrams, S., 2016. Eliminating electromechanical instability in dielectric elastomers by employing pre-stretch. J. Phys. D 49 (26), 265401.